EUROPEAN ORGANIZATION FOR NUCLEAR RESEARCH

CERN-EP/90-05
17 January 1990

ELECTROMAGNETIC DISSOCIATION OF 200 GeV/N ^{16}O and ^{32}S IONS IN NUCLEAR EMULSIONS

G. Baroni[8], V. Bisi[10], A.C. Breslin[3], D.H. Davis[6], S. Dell'Uomo[8], S. Di Liberto[8], P. Giubellino[10], G. Grella[9], K. Hoshino[7], M. Kazuno[4], M. Kobayashi[4], K. Kodama[5], A. Marzari-Chiesa[10], M.A. Mazzoni[2], F. Meddi[8], M.T. Muciaccia[1], K. Niu[7], L. Ramello[10], G. Romano[9], G. Rosa[8], C. Sgarbi[8], H. Shibuya[4], S. Simone[1], D.N. Tovee[6], N. Ushida[5], C. Wilkin[6] and S.K.C. Yuen[6]

ABSTRACT

This work represents the results of an experimental investigation of the electromagnetic dissociation of 200 GeV/N ^{16}O and ^{32}S ions in nuclear emulsions. Exclusive channels involving charged fragments have been studied as a function of the energy released, and, assuming a Weizsäcker–Williams spectrum of virtual photons, there is good agreement with results for the (γ,p) processes obtained with real photons. However the rates found for other processes are larger, in particular for the (γ,α) on both nuclei. The values of the total integrated absorption cross-sections are generally larger than those obtained from real photon experiments but the extent of the discrepancy depends strongly upon which photon results are used in the comparison.

Submitted to Nuclear Physics A

---

[1] Dipartimento di Fisica dell'Università and INFN, Bari, Italy.
[2] CERN, Geneva, Switzerland.
[3] Department of Physics, University College Dublin, Ireland.
[4] Department of Physics, Toho University, Funabashi, Japan.
[5] Aichi University of Education, Kariya, Japan.
[6] Department of Physics and Astronomy, University College London, UK.
[7] Department of Physics, Nagoya University, Nagoya, Japan.
[8] Dipartimento di Fisica, Università 'La Sapienza' and INFN, Rome, Italy.
[9] Dipartimento di Fisica Teorica e SMSA dell'Università and INFN, Salerno, Italy.
[10] Dipartimento di Fisica dell'Università and INFN, Turin, Italy.

1. INTRODUCTION

In collisions between two nuclei, the size of the impact parameter determines the character of the interaction. Strong-interaction processes dominate if the projectile and target overlap even marginally, whereas the interaction is purely electromagnetic for impact parameters that significantly exceed the sum of projectile and target radii. The relative contribution of the two types of process to the total interaction cross-section is a function of projectile, target, and energy, with electromagnetic processes expected to dominate the interaction of highly charged objects at high energies.

Cosmic-ray studies [1, 2] first illustrated this effect, and more systematic studies of both projectile [3–6] and target [7–11] electromagnetic dissociation were carried out when high-energy (a few GeV/N) ion beams became available.

Preliminary results, based on ^{16}O interactions with emulsion nuclei at 60 and 200 GeV/N, showed the dependence of electromagnetic effects on the incident particle energy [12], and further studies of the total charge-changing cross-section as a function of target, projectile, and energy [13–15] — up to 200 GeV/N — permitted the estimation of nuclear and electromagnetic contributions. The two were found to be nearly equal in the case of ^{32}S–Pb interactions at 200 GeV/N .

The results presented here refer to a systematic study, in emulsion, of the electromagnetic dissociation of ^{16}O and ^{32}S projectiles into different exclusive channels at an incident energy of 200 GeV/N . An estimate of the energy released in each interaction, and a model for the intensity and energy spectrum of the virtual photons, permits the determination of photoproduction cross-sections on oxygen and sulphur nuclei, up to the energy threshold for pion production, for most of the possible photoreactions. A comparison with results obtained for the same reactions with real photons is also made.

2. ELECTROMAGNETIC DISSOCIATION

In the model of Weizsäcker and Williams [16], the electromagnetic field of a point-charge target T is seen by a passing point-charge projectile P as a flux of virtual photons (fig. 1). The photon energy spectrum is computed classically as the Fourier transform of the time-varying electromagnetic field [17]:

$$\frac{dI}{d\omega} = \frac{2Z_T^2 e^2}{\pi c \beta^2} \left\{ x K_0(x) K_1(x) - \frac{\beta^2}{2} x^2 [K_1^2(x) - K_0^2(x)] \right\} \ , \tag{1}$$

where K_i are modified Bessel functions of order i, and $x = \omega b/(\beta\gamma c)$. Here b is the impact parameter, γ the Lorentz factor, and β the velocity of the incident charge in units of c. Putting the photon energy $E = \hbar\omega$, the maximum energy of the spectrum is

$$E_{max} \approx \frac{\hbar\gamma c}{b_{min}} \ , \tag{2}$$

where b_{min}, the minimum impact parameter, is in practice the sum of the radii of the colliding nuclei. Under our conditions, E_{max} ranges from 5 to 10 GeV, depending on the sizes of the projectile and target nuclei.

For $E \ll E_{max}$ (in practice, for $E < 0.2E_{max}$) and $\beta \simeq 1$, eq. (1) appropriately summed over the possible impact parameters can be approximated by

$$N(E) = \frac{2Z_T^2 e^2}{\pi \hbar c E} \left(\ln \frac{1.123 \hbar \gamma c}{E b_{min}} - \frac{1}{2} \right) \quad . \tag{3}$$

More recent approaches to the problem, based on quantum mechanical calculations, lead to essentially similar results for large values of γ, but with the photon spectrum distinguished by multipolarities. This will be discussed briefly in section 6.

It must be noted that nuclear emulsion is an heterogeneous target but, owing to the Z_T^2 dependence in eq. (3), the heaviest constituents (Ag and Br) contribute more than 95% of the total intensity. Figure 2 shows the low-energy part of the photon spectrum for ^{16}O projectiles of 200 GeV/N for the various constituents of the nuclear emulsion. The corresponding spectra for ^{32}S projectiles almost overlap the oxygen ones.

The response of the projectile nucleus to the flux of photons is governed by its photonuclear cross-section, which, to a first approximation, is proportional to Z_P. Depending on the energy of the incident quanta, the most effective absorption mechanisms are the giant dipole resonance for $10 < E < 40$ MeV, the quasi-deuteron effect for higher energies, and pion production above the corresponding energy threshold ($\approx$ 140 MeV). Absorption through the giant resonance usually leads to the emission of a single nucleon, leaving the residual nucleus either in the ground state or in some excited level. The kinetic energy of the fragments in the c.m. system is small, of the order of the binding energy of the ejected nucleons. The quasi-deuteron effect [18] becomes important as the photon energy increases, because the Fermi momentum of a single nucleon inside the nucleus is too small to satisfy the conservation of energy and momentum, and therefore an interaction with a cluster of nucleons is required. This mechanism favours the emission of more than one nucleon, and the total kinetic energy of the outgoing fragments is correspondingly larger than in the previous case. Above the threshold for pion production, the excitation of baryon resonances can contribute, and pions are emitted in addition to nuclear fragments. This process dominates at high energy.

Extensive studies of γ–nucleus cross-sections, especially those at lower energies, are often based on experiments designed to detect a single or a few channels, usually in an inclusive manner. Photonuclear cross-sections are also obtained through the inverse reactions, using detailed balance, or with activation techniques by detecting radioactive fragments in the final state.

In high-energy projectile dissociation, the fragments are confined within a forward cone that becomes smaller with increasing energy, and have a momentum per nucleon almost equal to that of the beam particle. There should be no evidence of excitation of the target nucleus. All possible configurations involving charged fragments can be detected easily and with high efficiency in nuclear emulsions and, in addition, measurement of the relative angles between fragments gives a reasonable estimate of the total kinetic energy.

Figure 3 shows the microphotograph of a complex example of projectile electromagnetic dissociation (EMD).

A flux of photons, similar to that experienced by the projectile, is seen by the target nucleus to originate from the projectile. In this case Z_T must be replaced by Z_P in eq. (3), and the target nucleus disintegrates according to its photonuclear cross-section. Such interactions give rise to the almost isotropic emission of low-energy fragments from the target, whilst the projectile continues undisturbed. Figure 4 shows the microphotograph of a probable example of such a process. The electromagnetic dissociation of target nuclei will not be considered further since, in general, the target remains unidentified and the scanning efficiency for such events is low.

Peripheral nuclear interactions may present the same topological features as those of projectile EMD events. In order to estimate such a contamination, a study of small but presumed hadronic interactions has been performed.

3. SEARCH IN EMULSION

Examples of projectile EMD were found in samples of events collected during a study of the general features of oxygen- and sulphur-emulsion interactions at 200 GeV/N . The standard scanning procedure, summarized below, was slightly modified to increase the efficiency for this particular class of events.

3.1 Exposures and scanning

Stacks of Fuji ET-7B emulsions, each comprising $\approx$ 60 pellicles of dimensions 16 cm $\times$ 5 cm $\times$ 600 μm, poured and assembled at CERN, were exposed to 200 GeV/N oxygen ions (1986) and sulphur ions (1987) in the H3 beam line of the West Area at CERN. The beam particles traversed the stacks parallel to the emulsion surfaces. The density of these emulsions, poured and dried at 70% relative humidity, was found to be (3.60 $\pm$ 0.01) g/cm^3, about 6% less than the 'standard' value [19].

Interactions were located using a line-scanning technique, whereby beam particles were picked up 10 mm from the entrance edge, and within the central 80% of the pellicle thickness, and were followed for a distance of 30 mm or until an interaction was found. In order to be efficient at finding projectile EMDs — in particular those where a single proton emitted at a very small angle to the beam becomes apparent only further downstream — apparently non-interacting particles were followed for an additional 10 to 20 mm. Figure 5 shows distributions of events as a function of their distance from the pick-up line: no loss is observed in any zone, and agreement with the expected exponential decrease is good.

The electromagnetic interaction between the projectile and the medium it traverses generally results in the ejection of very low energy electrons (δ-rays) and electron pairs, and increases rapidly with projectile charge. The majority of these can be recognized by eye (see figs. 3 and 4) and discarded, but tracks of electrons of medium or high energy (the tail of the distribution) can be identified in emulsion only when followed for a sufficient

length. This procedure would have increased the scanning time considerably. Therefore, in the case of topologies with just one or two minimum-ionizing particles, it was required that their emission angle θ be less than 5 mrad to the beam. This criterion eliminates (see section 4) almost all the high-energy knock-on electrons and most of the pairs, but no EMD candidate, in the selected range of photon energies. Once a nuclear interaction was found, the incoming track was carefully examined at higher magnification to ensure that it was indeed a beam track and not the tightly bunched fragments of an undetected EMD (see subsection 4.2).

Finally, for all the projectile EMD candidates, an accurate scan was performed upstream and downstream from the probable interaction point (uncertain to ± 1 mm or more in the most difficult cases) to check for the presence of previously undetected signs of a small nuclear interaction. At this stage, all interactions showing no target nuclear excitation ('black' and 'grey' prongs) and with all tracks emitted within 5 mrad to the beam were considered as candidates for projectile EMD, and the remainder as strong interactions. A full account of the properties of nuclear interactions found in this search will be presented elsewhere [20].

Some 13,000 tracks of 200 GeV/N ^{16}O and 8,000 tracks of 200 GeV/N ^{32}S nuclei were followed. The total path lengths, and the numbers of nuclear interactions and projectile EMD candidates are shown in table 1. Also included are results from the scanning of secondary projectile fragments [20] with charges $2 \leq Z \leq 7$ performed on a sample of oxygen-emulsion interactions. Nuclear interaction and projectile EMD mean free paths in emulsion are shown in fig. 6. It is easily seen that, as expected, the mean free path for EMD decreases from He to O to S much faster than that for nuclear interactions.

Table 2 shows numbers and relative rates for the visible channels from ^{16}O and ^{32}S EMD, classified according to their topology, for different ranges of energy (see subsection 3.4). Although the data are raw (see section 4 for corrections), some global features are evident. Among them is the fact that the emission of a single hydrogen isotope (in most cases probably a proton) is the dominant process in both samples, with a rate of $\sim 55\%$. The emission of two protons, on the contrary, is considerably more frequent in ^{32}S than in ^{16}O EMD, whereas the situation is reversed when considering the emission of a single He isotope. Finally, the proportion of higher-energy events increases with increasing multiplicity in the final state. This is particularly evident in the channels containing only He and H isotopes in the oxygen sample. The fact that the events that exhibit higher energy releases are populated by complex break-up modes of the projectile nuclei and not by the emission of one energetic fragment might indicate that these events could be associated with multiphoton absorption processes [12].

3.2 Angle and charge measurements

The angles of outgoing fragments relative to the heaviest one were obtained by measuring relative distances between tracks at increasing distances from the interaction point, typically in the range from 10 to 40 mm. Plane (α) and dip (δ) angles were

computed by fitting the trajectories to straight lines through the measured coordinates. Assuming an error of ~ 0.5 μm in the coordinates, the space angles are accurate to within 0.05 and 0.10 mrad, including the error due to multiple scattering, except in a few cases where one of the outgoing fragments interacted after a short distance.

Figures 7a,b show plots of the relative separation angles $\Delta\alpha$ and $\Delta\delta$ for the categories O $\rightarrow$ NH and S $\rightarrow$ PH. These categories, involving the emission of a single minimum-ionizing particle and of a fragment differing by one unit of charge from the primary, are expected to be the ones most seriously affected by scanning losses. For uniform detection efficiency, the different sectors of the plots should be equally populated. This is indeed true, within statistical errors, in the oxygen sample (fig. 7a), but in the sulphur sample (fig. 7b) a $(9 \pm 3)\%$ loss of events is found to occur in planes steeply inclined to the plane of the emulsions. The loss is to be expected in the sulphur sample because phosphorus tracks have a much higher δ-ray density than nitrogen tracks (in the ratio 4.6:1), and this masks a minimum-ionizing track more easily when it is almost superimposed on the ion track. In addition, the relative change in δ-ray density is much less noticeable from S $\rightarrow$ PH than from O $\rightarrow$ NH.

Events in the other categories, involving a higher number of outgoing tracks (for example O $\rightarrow$ CHH, S $\rightarrow$ MgHeHH, etc.), or those with a larger difference between the charge of the heaviest fragment and that of the primary (such as O $\rightarrow$ CHe or S $\rightarrow$ SiHe) are much more easily detected. Plots similar to those shown in figs. 7a,b indeed suggest that in these cases the corresponding detection efficiencies are much closer to 100%.

Charge measurements were performed on projectile EMD candidates and on a sample of nuclear interactions by determining the relative density of δ-rays along the beam track and each of the outgoing fragments. It was possible to determine, by eye, the charge of fragments with $Z = 1$ and $Z = 2$ (see fig. 3), and therefore systematic charge measurements were performed only on fragments with $Z > 2$. A sample of fragments with $Z = 2$ was also measured, and in all cases the previous judgement turned out to be correct.

The linear density of δ-rays for a particle with $\beta \approx 1$ is

$$\frac{dn}{dx} = aZ^2 \ , \tag{4}$$

with $a \approx 1/\text{mm}$ in nuclear emulsion [19]. The exact value of a depends on the operative definition of a δ-ray, in practice on the accepted minimum range—and thus energy—of the ejected electrons. It is relatively easy to count individual δ-rays on tracks up to $Z \approx 10$, but for higher values of the charge the δ-ray density becomes too large and it is no longer possible to disentangle single, scattered electron tracks. In such cases it was better to measure P_0, the frequency of observing no δ-ray in a given sequence of consecutive cells of length t [21]:

$$P_0 = e^{-aZ^2 t} \ , \tag{5}$$

where the value of a is the same as in eq. (4) if the same convention is used. The error in the charge measurement can be shown to be

$$\delta Z = \frac{k}{2}(aL)^{-\frac{1}{2}} \tag{6}$$

where L is the total length considered. The value of k is 1 with the first method (this is the minimum statistical error), whereas it depends on P_0 in the second [22], being $k \leq 1.3$ for $P_0 \geq 0.4$.

Typical charge spectra, obtained by counting δ-ray densities (fig. 8) and δ-ray gaps (fig. 9) on primary and secondary tracks, show a dispersion on individual charges in agreement with that expected from the measured length L, usually 2 to 5 mm. It is seen that the accuracy is good enough to detect, unambiguously, differences of one unit of charge around $Z = 8$ and two such units around $Z = 16$.

3.3 Estimate of the energy

Projectile EMDs involving the emission of neutrons alone are not detectable, and those where one or more neutrons are emitted with other fragments are misidentified. In addition, only the charges but not the masses are determined.

In this experiment, neither the energy nor the momentum of a high-energy particle can be determined, but an estimate of the total c.m. kinetic energy E released in the interaction was made by assigning, to each fragment, a mass according to its charge and a momentum per nucleon equal to that of the beam. The following rules were adopted:

a) when only one or two minimum-ionizing particles are seen, they are assumed to be protons, and neutron emission is not considered. Thus only channels $^{16}\mathrm{O} \rightarrow {}^{15}\mathrm{Np}$ or $^{16}\mathrm{O} \rightarrow {}^{14}\mathrm{Cpp}$, and $^{32}\mathrm{S} \rightarrow {}^{31}\mathrm{Pp}$ or $^{32}\mathrm{S} \rightarrow {}^{30}\mathrm{Sipp}$ are taken into account;

b) in all other cases it is assumed that $A = 2Z$ (including $Z = 1$). The only exception is the channel O $\rightarrow$ BHeH, taken to be $^{11}\mathrm{B}\alpha\mathrm{p}$ (see subsection 5.3).

In order to estimate E, all the measured angles θ_i are transformed into angles θ_i' with respect to the direction of the centre of mass of the charged fragments. The components of momentum transverse to that direction are computed ($p_{T_i} = p_i\theta_i'$), and, assuming isotropy,

$$E = \sum E_i = \frac{3}{2}\sum \frac{p_{T_i}^2}{2m_i}. \tag{7}$$

Rule (b) essentially states that the average number and average energy of the undetected neutrons are equal to those of the detected protons; it does not imply that all protons and neutrons are emitted as deuterons. The bias introduced by rule (a) will be analysed in section 5, as well as the hypothesis of isotropy.

Figure 10 shows the energy spectra computed in this way for the different channels observed in the projectile EMD of oxygen nuclei. The spectra involving B, Be, and Li isotopes as the heaviest outgoing fragment have been grouped, irrespective of the number of He and/or H isotopes.

4. RAW DATA AND CORRECTIONS

In this section we will examine the analysis carried out to remove spurious events and to correct for biases and losses. It will be shown that in general the overall corrections represent only a small fraction of the signal.

4.1 Spurious events

Spurious events are expected to be mainly due to knock-on electrons, electron pairs, and peripheral hadronic interactions.

Energetic knock-on electrons are produced with a large cross-section [23] when a relativistic projectile (assumed to be a point-charge) passes through a medium. The electron energy spectrum is

$$\frac{dN}{dE} = k\frac{Z_P^2}{E^2}\left(1 - \frac{E}{E_{max}}\right) \ , \tag{8}$$

where the maximum energy of the ejected electrons ($E_{max} \approx 2mc^2\gamma^2$) is about 40 GeV in our conditions.

The angular distribution of the knock-on electrons, however, is wide:

$$\tan\theta \simeq [E(\mathrm{MeV})]^{-\frac{1}{2}} \ , \tag{9}$$

and the cross-section tends to zero in the very forward direction.

In the case of 200 GeV/N ^{32}S ions, the number of knock-on electrons per centimetre of track, making an angle $\theta < 100$ mrad with the beam, was observed to be 1.5. Therefore, the overwhelming majority of knock-on electrons would have been removed at the scanning stage by the criterion that the maximum separation angle be $\theta < 5$ mrad (see section 3). There were, however, some tens of cases, in both oxygen and sulphur samples, where a single minimum-ionizing track emitted at $\theta < 5$ mrad was observed to scatter appreciably — behaviour expected from an electron losing its energy by bremsstrahlung. Events containing such tracks were also rejected, either at the scanning stage or after the angular measurement. No loss of genuine events is expected from this procedure, because at this energy both multiple scattering and visible bremsstrahlung are exceedingly small for nuclear fragments.

After these cuts, the measured charge of the heavier fragment of all remaining candidates in the O $\rightarrow$ NH channel was compatible only with $Z = 7$, thus showing that there was no further contamination in the sample. It is therefore assumed that application of the same criteria to the sulphur sample removes the background from knock-on electrons in that case also. Fragment charge measurements are more time consuming and less accurate for the heavier fragments from sulphur dissociation and the charges of fragments in the S $\rightarrow$ PH channel have been determined for only a fraction of candidates.

Electron pairs are created by photons in the Coulomb field of both the projectile and the target nuclei. The shape of the energy spectrum [eq. (3)] means that they are mainly low-energy pairs in the frame of reference of the respective nucleus, but those

created in the field of the projectile tend to become energetic and are collimated with the incident beam particle in the laboratory system [24]. In the case of 200 GeV/N ^{32}S ions, about 0.1 electron pairs per centimetre of track were observed at angles $\theta < 100$ mrad to the primary. This is consistent with preliminary results from EMU04 [25]. Most of the electron pairs were rejected at the scanning stage by the angular requirement $\theta < 5$ mrad. The remainder — a few cases in each sample — where one or both tracks were observed to scatter appreciably, were eliminated either at the scanning stage or after the angular measurement. At most, very few cases of undetected electron pairs are thus likely to have been included in the samples. They cannot be distinguished from coherently produced pions, and are therefore treated as such. In any case there will be no confusion with EMD events of the type Cpp or Sipp, since δ-ray measurements are well able to discern a charge change of two.

Peripheral nuclear interactions may simulate a projectile EMD if there is no appreciable excitation of the target and if all the fragments from the interaction are confined within a narrow forward cone. The total number of spurious events was conservatively estimated by taking the number of events with evaporation prongs $n_H > 0$ ('heavy' tracks in emulsion), but otherwise simulating a projectile EMD, and scaling it to represent the contribution from the total sample. The scale factor was taken to be the fraction of interactions with $n_H = 0$ ('white' stars) among those with a small number of secondary particles (n_s). The details of this procedure are shown in table 3; the fraction of white stars has been computed for $6 \leq n_s \leq 10$ (for $6 \leq n_s \leq 12$ in the S sample) to avoid biases introduced by the scanning criteria. The numbers of spurious events to be expected are then 16 ± 6 and 18 ± 7 in the oxygen and sulphur samples, respectively.

Although a correlation between n_H and n_s has been shown to exist [20, 26], it is expected that for small values of n_H and of n_s these two numbers are essentially uncorrelated. Therefore, the fraction of spurious events simulating EMDs in both energy and topology was taken from subsamples of events with $n_H > 0$ and $n_s \leq 6$ outside $\theta = 5$ mrad, considering the tracks within $\theta = 5$ mrad as if they were the only fragments. Table 4, like table 2, shows the results of this analysis. Here, the energy was computed as for true EMDs, except in the case where a single heavy fragment (f) was present. The analogous EMD is, in fact, undetectable, being the emission of neutrons alone.

The main differences between this sample and the one arising from true EMDs are the smaller fraction of events in which a single H isotope is emitted (with a corresponding increase in the fraction of complex channels) and the way in which the energy is shared. In table 5 the spurious events are shared among the corresponding channels as a function of the energy. It is readily seen that the average contamination is likely to be small for $E < 150$ MeV (2% to 3%), but increases to $\sim 20\%$ and to $\sim 50\%$ for $E > 150$ MeV and $E > 500$ MeV, respectively.

In these calculations no use was made of the charge measurements, because the presence of charged tracks outside the angular acceptance influences the total charge

inside. For the EMDs there was a final constraint that, to within errors, the sum of the measured charges of all outgoing fragments be

$$\sum |Z_i| = Z_P \ , \tag{10}$$

where Z_P is the charge of the projectile. The error for $Z \leq 2$ was taken to be zero. This constraint very efficiently removes the possible background arising from coherent production and residual electron pairs without loss of true signal (see subsection 3.2, measurement errors).

4.2 Loss of events

A projectile EMD may be lost or misidentified if it is followed by a nuclear interaction or by a further EMD that occurs before all the outgoing fragments are resolved. The size of the effect depends on the particular channel and on the angular distribution of the fragments. The situation is sketched in fig. 11, where the most likely contributions (either losses or gains) are considered for the channel S $\rightarrow$ PH. The main 'gains' come from more complex EMDs in which a successive nuclear interaction occurs at a stage when one H track is apparent but the remaining fragments are not resolved. In principle, the situation could be clarified by a charge measurement, but the unavoidable presence of other close tracks (and often the short path) does not allow a precise estimate.

In order to determine the contribution of these effects to the various channels, it was assumed that an EMD event would not have been detected if the relative separation of the outgoing tracks, perpendicular to the beam direction, lies within an ellipse of semi-axes $\Delta y = 0.5$ μm in the plane parallel to the emulsion surface and $\Delta z = 1.5$ μm in the perpendicular plane, for the oxygen sample. Because of the higher density of δ-rays, these quantities have been increased to 1.0 μm and to 3.0 μm, respectively, for the sulphur sample. Nuclear interaction and projectile EMD mean free paths have been taken (or interpolated) from those shown in fig. 6 and in table 1.

Table 6 shows raw and corrected data for the different samples in the lowest range of energy: E < 150 MeV. In the oxygen sample, the correction factors roughly compensate within this energy range, whereas in the sulphur sample the overall effect is an average loss of events of about 4%.

It was shown in subsection 3.3 that a loss of (9$\pm$3)%, corresponding to (24$\pm$8) events, is present in the channel S $\rightarrow$ PH of the sulphur sample. It is found that the loss due to nuclear interactions does not lead, globally, to the observed selective loss of events when both fragments are contained in a plane that is steeply inclined ($>60°$) to the emulsion plane, and therefore the two contributions will be treated independently.

The scanning loss, as can be seen in fig. 7b, occurs for opening angles $\Delta\theta < 0.5$ mrad, and thus for energies E < 8 MeV. It has been accounted for by adding the missing events in proportion to those present in the $\Delta\delta$–$\Delta\alpha$ plane in the unbiased region. Figure 12 shows corrected energy spectra for the channels observed in the sulphur sample. Corrections are noticeable only in the lower-energy bins.

5. ANALYSIS OF SINGLE CHANNELS

5.1 General features

The two sets of data shown in figs. 10 and 12 and in tables 2 and 6, obtained with oxygen and sulphur projectiles, have some features in common. For example, the emission of a single H isotope is the dominant process in both cases, and shows a similar energy spectrum. However, although the energy spectrum for a single He isotope is similar in the two cases, the production rates are somewhat different. Two H isotopes are emitted with very different rates, and the shapes of their energy spectra are also different. When more complex channels are considered, the energy spectra are systematically harder in the S samples.

Some of these differences can readily be understood by taking into account the different nature of the projectiles and the different Coulomb barriers. Oxygen, with a binding energy of 128 MeV, can disintegrate into 21 channels, each with outgoing fragments of different individual charges, and 16 of these channels have been observed. Sulphur, with a binding energy of 272 MeV, can disintegrate into more than 200 such channels, of which only 28 have been observed. As more complex channels have, in general, a higher photoproduction threshold (with some obvious exceptions, like $^{16}O \rightarrow 4\alpha$), they are more depressed in the sulphur sample than in the oxygen one, owing to the shape of the photon spectrum (fig. 2). Table 7 shows the separation energies of various combinations of fragments from oxygen and sulphur, as deduced from atomic mass excesses [27]. These are also the minimum energy thresholds for the corresponding photoproduction reactions.

It is clear that some of the assumptions made so far will not be valid in all circumstances. For instance, in the channels that involve the emission of a single minimum-ionizing particle assumed to be a proton (subsection 3.3), some contribution from $^{16}O \rightarrow {}^{14}Npn$ and from $^{32}S \rightarrow {}^{30}Ppn$ could be present. However, as already pointed out, this experiment is not sensitive to isotopic differences so that there could be some contribution, for example, of $^{16}O \rightarrow {}^{12}Ctp$ or $^{16}O \rightarrow {}^{13}Cdp$ events in the ^{14}Cpp sample.

5.2 Channels involving two nucleons

The fact that energy spectra of events in the HH channels are considerably harder than the corresponding ones where a single proton is emitted, suggests that a correlation might exist between the outgoing protons. In order to check this hypothesis, the azimuthal angle φ between the minimum-ionizing particles, computed in the c.m. system of the excited nucleus, was plotted as a function of energy, as shown in figs. 13a and 13b for the oxygen and sulphur samples, respectively. No correlation is observed in either sample in any energy range, within the statistical errors.

Furthermore, no correlation is observed between the energies of the outgoing protons. In particular, in the subsamples of the most energetic events ($E > 35$ MeV), the energy is preferentially taken by one of the particles, whereas the other one behaves like that emitted in the channels with a single proton. This fact is illustrated in figs. 14, where each event of the CHH or of the SiHH samples has been treated like a NH or a PH pair,

respectively, each time neglecting one proton. The energy spectra thus obtained (with each event now counted as 0.5 events) are indeed similar to those of the corresponding single-proton distributions in figs. 10 and 12. This would suggest uncorrelated emission of the protons in the energy range considered here.

Any pn contribution is unavoidably included in the appropriate single-proton channels. If the pn pairs were emitted with characteristics similar to those of the pp pairs considered above, visible energy distributions similar to those shown in fig. 14 would then be expected. Whilst it would be tempting to interpret the tail of events with $E > 40$ MeV in the NH and PH samples as being due to pn contamination, the subtraction of spectra normalized to such a low number of events would be too unreliable. We will for the moment ignore this contamination, which in any case (see section 6) will be shown to be small.

5.3 Integrated energy spectra and angular distributions

Figures 15 and 16 show integrated energy spectra for the most abundant channels in the low-energy region ($E < 70$ MeV). As most of the BHeH events have rather low energy (fig. 10), it seemed more reasonable to treat them as ^{11}Bαp rather than as ^{10}Bαpn (see subsection 3.3).

All the distributions are seen to decrease with energy in a roughly exponential manner, with some possible Coulomb barrier effects at very low energy. They thus resemble evaporation spectra, and the corresponding temperatures ($T = 8$ to 10 MeV) are quite similar in both the oxygen and sulphur samples, when a single fragment, either a H or a He isotope, is emitted. Higher values of the temperature are found when more complex channels are considered.

Table 8 shows the values of the fitted inverse slopes T from an exponentially decreasing energy spectrum cut at a maximum energy E_1 to avoid any contribution from anomalous tails. Both the temperature and the errors were determined by means of the maximum likelihood method. The expected number of events above E_1 was then computed from T and the value of the number of events observed in the energy range up to E_1, and was used in figs. 15 and 16. It can be seen that the values of T, when corrected for the c.m. angular distribution (see below), are of the same order of magnitude as the separation energy of the respective fragments from the original nucleus. In particular, there is a trend for the sulphur spectra to be softer than the corresponding oxygen ones, in agreement with the same trend in the separation energies (table 7). An exception already noted is the Bαp channel, which shows a much softer spectrum than was expected; moreover, this situation would not be changed by considering the events as Bαpn.

Energy spectra reconstructed from transverse momenta are distorted with respect to the original spectra, and the average value of the 'transverse' energy thus obtained depends on the angular distribution. Figure 17 shows the shape of the transverse energy spectra (dN/dE' versus E') for a two-body reaction, reconstructed from a monochromatic spectrum (E^*) in the c.m. system, but with different angular distributions ranging from

those peaked in the forward direction to those peaked at 90° to the beam. The lowest-energy part of the spectrum is seen to be particularly sensitive to the angular distribution. Thus, if the distribution is other than isotropic, we will obtain a biased estimate of the average energy.

For more complex c.m. energy spectra, the reconstructed energy distributions are accordingly more complicated. Having shown in figs. 15 and 16 that the experimental distributions decrease exponentially, we computed, as an example, how an energy spectrum of the form

$$\frac{dN}{dE} = \begin{cases} T_0^{-1}\exp[-(E-E_s)/T_0] & \text{for } E \geq E_s \\ 0 & \text{for } E < E_s \end{cases} \tag{11}$$

in the c.m. system transforms into the lab. system when the angular distributions quoted in fig. 17 are considered and the energy scale is adjusted for isotropic emission.

Equation (11) represents a rough approximation to an evaporation spectrum with a sharp energy threshold E_s. The result of such a calculation is shown in fig. 18a for the values $E_s = 3.5$ MeV and $T = 7$ MeV. It is found that for $E \gg T$, all the distributions in the lab. system would decrease exponentially with an inverse slope $T = 1.5T_0$. However, in the energy range $2E_s < E < 3T_0$ the curve is steeper, giving $T = (1.05 \text{ to } 1.2)T_0$, which is much closer to that of the c.m. distribution; for $E < E_s$, the shapes of fig. 17 are essentially reproduced.

From these considerations, the c.m. spectrum given by eq. (11), with $T_0 = 9$ MeV and for different values of E_s, has been transformed assuming isotropy and compared with the experimental data of the channel O $\rightarrow$ Np. The best agreement is found for $E_s = 1.5$ MeV (fig. 18b); the other distributions lead to much poorer results. Similar trends are observed for the other two-body channels.

We therefore conclude that it would be very difficult, with the present statistics, to extract c.m. angular and energy distributions from the experimental data. These calculations, however, show that the hypothesis of isotropic emission in the c.m. system is indeed plausible. It is also seen that reasonable shapes of the two-body c.m. energy spectra are well reproduced, except for an obvious distortion in the very low energy bins.

In the case of three or more fragments in the final state, the energy estimated from eq. (7) is expected to be more reliable not only as an average but also for single events. Correspondingly, the values of T_0 given in table 8 were obtained from T by multiplying by a factor of 2/3.

6. EMD AND PHOTOPRODUCTION CROSS-SECTIONS

6.1 Nuclear and EMD cross-sections on silver

In order to obtain absolute cross-sections and to compare our results with other high-energy data, we transformed interaction lengths in emulsion into absolute cross-sections on silver, the heaviest abundant constituent of the emulsions. Throughout this work the presence of elements such as iodine, whose abundance is less than 1%, and of other elements present in even smaller proportions, has been neglected.

Using the actual density of the emulsions (subsection 3.1) and assuming that the difference between that value and the 'standard' emulsion density [19] is merely due to an increased water content, it is estimated that the density of silver is

$$N = 93 \times 10^{20} \text{Ag atoms per cm}^3 \ . \tag{12}$$

The total nuclear cross-sections are then computed from the interaction lengths in emulsion and from the number f of interactions on silver as a fraction of the total number of emulsion interactions [20]:

$$\sigma = \frac{f}{\lambda N} \ . \tag{13}$$

The projectile EMD cross-sections are computed in a similar way, by taking into account the appropriate value of f (see fig. 2). In the following, the corrected values of the number of events — hence of the interaction lengths — have been used, rather than those quoted in table 2.

Table 9 shows experimental results from the present search and from other experiments at the same energy [13, 14, 28] where, in general, the charge-changing cross-sections are measured. There is a good overall agreement on both nuclear and EMD cross-sections, despite the quite different methods used to derive the latter. In emulsion, nuclear and EMD contributions are measured separately, and a scaling factor is used to take into account the inhomogeneous nature of the target. In the other experiments, the pure nuclear cross-section, being almost energy independent, is obtained in substance from low-energy data and subtracted from the total charge-changing cross-section to give the cross-section for EMD. In refs. [13] and [14], factorization rules were also applied to give an overall fit. In our data on the total σ_{EMD} (labelled 'no cut' in table 9), the contribution due to pion photoproduction has been excluded by the scanning and analysis criteria.

It is also interesting to look at partial cross-sections for the production of a given fragment of charge Z_F as the heaviest outgoing fragment. Table 10 shows our results and those from refs. [13] and [14]. It should be noted that the sulphur data from ref. [14] were obtained from the formula suggested in their text, $\sigma_{EMD}(P,T,F) = \epsilon_{PT}\,\epsilon_P^F$, where the values of ϵ_{PT} and of ϵ_P^F quoted in their tables were used. However, the fact that ϵ_{PT} has been arbitrarily normalized to 1 for a carbon target makes the absolute scale of these cross-sections somewhat uncertain, and therefore no value for $Z \leq 7$ is quoted.

In both samples, the channels involving fragments with a charge differing by one and two units from that of the projectile account for more than 80% of the total EMD cross-section. Therefore, when the high-energy tail of the photon spectrum is included, the relatively large increase in the partial cross-sections for the production of charges that are very different from the charge of the projectile has little effect on the total cross-section.

6.2 Photoproduction cross-section

Photoproduction cross-sections for exclusive reactions may be evaluated from the corresponding energy distributions and from the energy spectrum of the virtual photons:

$$\sigma_\gamma(E) = \frac{1}{N(E)} \frac{d\sigma_{EMD}}{dE} \ , \tag{14}$$

where $N(E)$, given by eq. (3), is shown in fig. 2 for an emulsion target; σ_{EMD} for a given channel is obtained as in eq. (13), but with all the quantities referred to the whole emulsion. Both $\sigma_\gamma(E)$ and its integral up to a given energy E_0, $\sigma_{int}(E_0)$, can then be compared with the corresponding values measured with low-energy real photons.

Obviously, the energy E of the quanta that produce a given reaction appears as the sum of the c.m. kinetic energy and of the binding energy of the outgoing fragments, but may also contribute to the excitation energy of the residual nucleus. In the following, we will assume that the residual nuclei remain in their ground state for all reactions, and that the energy spectra obtained through eq. (7) are the true energy spectra (we have shown in subsection 5.3 that this is valid only on the average). This procedure implies that, in order to obtain $\sigma_{EMD}(E)$, each distribution shown in figs. 10 and 12 must be shifted towards higher energies by an amount corresponding to the threshold of the respective reaction (table 6).

It should be noted that neglect of the excitation energy of the residual nuclei implies an average underestimation of the photon energies and therefore, owing to the $1/E$ dependence of the virtual photon spectrum, an underestimation of the corresponding $\sigma_\gamma(E)$. However, the energy spread introduced by the estimate of E from p_T (subsection 5.3) leads to an effect in the opposite direction. Hence, there is at least a partial compensation between these two effects.

Figures 19 and 20 show cross-sections obtained in this way, both for specific reactions (σ_γ) and summed over all those detected (σ_γ^{ch}) from oxygen and sulphur EMD, for photon energies up to 150 MeV. As a general comment, we note that in both cases the giant resonance peak lies in the expected position (at a lower energy in sulphur than in oxygen), but is broadened by the energy estimate procedure. Obviously, the contributions from (γ,n) and (γ,nn) reactions should be added to σ_γ^{ch} in order to obtain the total photoabsorption cross-sections.

As seen in fig. 19, in oxygen a few reactions contribute mainly to the giant resonance region, namely (γ,p), (γ,α), and (γ,4α). The reactions (γ,pp) and (γ,αp) contribute appreciably both to the giant resonance and to the intermediate energy regions, whereas all the other reactions contribute only to the region with $E > 50$ MeV.

The situation in sulphur, as seen in fig. 20, is simpler than in oxygen because fewer reactions contribute up to 150 MeV. In detail, (γ,p) and (γ,α) contribute essentially only in the giant resonance region; (γ,pp) contributes also in the region with $E > 50$ MeV. Of the remaining 25 reactions (81 events), only five contribute in the region $E < 150$ MeV.

Table 11 shows integrated cross-sections $\sigma_{int}(E)$ for various ^{16}O photoreactions (up to 140 MeV) obtained in the present work. Also shown are the integrated photoabsorption cross-section from Ahrens et al. [29] and data on the most abundant reactions from other works [30–33]. The normalization of photoabsorption cross-sections is far from trivial [34] and the recent review by Fuller [33] suggests strongly that the Ahrens et al. [29] values of the total absorption cross-section up to 40 MeV should be reduced by a factor of about 1.4. There is agreement between the original data of Ahrens et al. [29] and ours when account is taken of the (γ,n) process not seen in this experiment. However, if the total cross-sections obtained from the summation of partial ones are considered the more reliable [33], our analysis in terms of single-photon exchange would indicate that our total absorption cross-section is some 40% larger than expected. The integrated cross-section for the reaction (γ,p) does, however, compare well with previous results in the giant resonance region. Above that, an overestimate is observed, and this is probably due to the fact that it includes also the reaction (γ,np), whose contribution, very small at lower energies, increases appreciably with increasing energy: $\sigma_{int}(170) = 60$ MeV·mb [30].

The comparison with results from single photoreactions is not straightforward. Often a single or very few reactions are observed in a given experiment, normally within a limited energy range. Furthermore, photoneutron cross-sections usually include reactions with charged particles as well. On the other hand, this experiment does not observe neutron emission, nor does it distinguish between various isotopes.

However, there are three reactions with characteristic final states but with comparatively small integrated cross-sections $\sigma_{int}(E)$ with values as follows:

$$
\begin{aligned}
^{16}\mathrm{O}\ (\gamma,\alpha)^{12}\mathrm{C} \quad & \sigma_{int}(40) = (21 \pm 4)\ \text{MeV·mb}\ , \\
^{16}\mathrm{O}\ (\gamma,\alpha\,\mathrm{p})^{11}\mathrm{B} \quad & \sigma_{int}(50) = (13 \pm 4)\ \text{MeV·mb}\ , \\
^{16}\mathrm{O}\ (\gamma,4\alpha) \quad & \sigma_{int}(50) = (4.2 \pm 2.5)\ \text{MeV·mb}\ .
\end{aligned}
$$

The integrated cross-section of the reaction (γ,4α), although based on a very few events, is perfectly consistent with the value obtained for real photons: $\sigma_{int}(30) = 5$ MeV·mb [30] and $\sigma_{int}(40) = 3.7$ MeV·mb [33]. Previous results on the reaction $(\gamma,\alpha\,\mathrm{p})$ gave $\sigma_{int}(55) = (4.8 \pm 0.4)$ MeV·mb [35]. Taking the errors into account, our result, although higher, is not inconsistent with that number, and confirms that a reaction producing such a pronounced break-up of the nucleus contributes appreciably at low energy (see subsection 5.3). Finally, in previous works [33] the reaction (γ,α) was found to have $\sigma_{int}(29) = 2.2$ MeV·mb, contributing almost exclusively through narrow peaks around 12 to 14 MeV. This result is based on measurements of inverse (α,γ_0) capture reactions, but direct measurements [30, 36] give similar values.

The low value of σ_γ for the (γ,α) reaction, despite the low-energy threshold, is explained by the isospin selection rule $\Delta T = 1$ for E1 photon absorption. For $\sigma_{int}(40)$ we find a value an order of magnitude larger than that for real photons, mainly at low energies.

As we have neither isotope separation nor efficient neutron detection, contamination from other reactions could well be included in our (γ,α) data, for example $(\gamma,^3\mathrm{He})$ and $(\gamma,\alpha\,\mathrm{n})$. The reaction $(\gamma,^3\mathrm{He})$, based on measurements of the inverse $(^3\mathrm{He},\gamma_0)$ capture reaction, has $\sigma_{int}(36) = 0.75$ MeV·mb [33] and this would correspond to the observation of one event under our conditions, when the appropriate value of the energy threshold ($B = 22.8$ MeV) is taken into account. If the same reaction were interpreted as (γ,α), it would yield $\sigma_{int}(20) = 0.3$ MeV·mb, which is clearly negligible. On the other hand, $(\gamma,\alpha\,\mathrm{n})$ was found [37] to have $\sigma_{int}(55) = (4.1 \pm 0.4)$ MeV·mb and, using similar arguments, it would give about three events and $\sigma_{int}(40) = 2$ MeV·mb when interpreted as (γ,α) under our conditions. Even if we assume that for the reaction $(\gamma,\alpha\,\mathrm{n})$ the contribution is equal to the one found for $(\gamma,\alpha\mathrm{p})$, the contamination would be of 10 events and $\sigma_{int}(40) =$ 6 MeV·mb. A more uncertain contribution to the background could come from the reaction $(\gamma,^3\mathrm{He\,n})$. If this were significant it would suggest that some events classified as $(\gamma$,pp) might in reality be $(\gamma$,tp).

Corrections to the Weizsäcker–Williams picture are necessary since the photons are virtual and not real. Real photons must be considered as plane waves, with an equal weight from all possible multipolarities (E1, M1, E2, ...), and the spectrum described by eq. (1) is of this kind. Using a different approach, however, other authors [38–42] derived virtual photon spectra in ion collisions distinguished by multipolarities. Whilst the E1 and M1 spectra are almost coincident with the classical ones when $\beta \rightarrow 1$, the E2 spectrum differs considerably in the low-energy region. In this limit there is an additional term of the form [41]

$$2K_1^2(x)/\gamma^2 \tag{15}$$

in eq. (1), which raises the E2 intensity with respect to E1 by a factor of 3.2, 1.6, and 1.3 for $E = 10$, 20, and 30 MeV, respectively. This fact has been accounted for when computing total photonuclear cross-sections for comparison with EMD cross-sections, by applying a small overall correction factor [8, 10, 13, 14].

In the case of the (γ,α) reaction on oxygen we must expect a higher correction factor because the cross-section for E1 photon absorption is depressed and, as a consequence, the E2 contribution becomes a larger fraction [33]. Hence, both this fact and the low value of the threshold conspire towards making this reaction particularly sensitive to a different admixture of multipolarities. It is, however, estimated that this effect could hardly raise the integrated cross-section measured with real photons by a factor of 2, and thus the high value found in the present experiment remains largely unexplained.

We note that in the analysis of electrodisintegration of nuclei done by Martins et al. [43] using DWBA virtual photon spectra, a similar effect is found. Here again, the E2 virtual photon spectrum is enhanced with respect to the E1 spectrum.

Table 12 shows the integrated cross-sections for sulphur, presented in the same form as the oxygen ones in table 11. The comparison with other data is more difficult in this case. The total absorption cross-section results of Wyckoff et al. [44] were used up to

E = 35 MeV. Above this value, the lack of data has been filled by interpolating results from Al and Ca [29]. Results from reactions (γ,n) and (γ,np) [45, 46] have been added, up to E = 60 and 80 MeV, respectively. Here, as in oxygen, the contribution from (γ,np) is much smaller than that observed for (γ,p) in the giant resonance region; above, it is not known. There is some discrepancy in previous results obtained between the thresholds for the reactions (γ,p) and (γ,n): whereas Wyckoff et al. [44] find almost no contribution from this zone in the total absorption cross-section, Dolbilkin et al. [47] find $\sigma_{int}(15)$ = 75 MeV·mb and estimate $\sigma_{int}(30)$ = (275±70) MeV·mb for the reaction (γ,p). Both these values agree roughly with our result.

When the undetected yield from the reaction (γ,n) is accounted for [$\sigma_{int}(40)$ = 130 MeV·mb], good agreement is found for E < 50 MeV but with possibly an excess above that energy. The interpolated data must, however, be regarded with some caution.

For the reaction (γ, α) there is a discrepancy that is very similar to the one found for oxygen. Now $\sigma_{int}(30)$ = (28±6) MeV·mb, whereas the integrated cross-section (from 13 to 19 MeV) deduced from measurements of the inverse (α, γ_0) capture reaction gives σ_{int} = 1.4 MeV·mb [48]. Here again the reaction should be suppressed and an enhanced contribution from the E2 virtual photon spectrum is insufficient to explain the result.

Another possible explanation for the high rate of the (γ, α) reaction could be in terms of multiphoton absorption, since $0^+ \underset{\rightarrow}{\alpha} 0^+$ transitions are easily accessible to two-photon processes. It is clear that within the model of Baur and Bertulani [49], in which the photons in the pulse are considered incoherent, when a relativistic oxygen or sulphur ion impinges even on a silver nucleus, the chance that two photons will be absorbed is very small. However, the passage time of these ultrarelativistic ions through the Lorentz-contracted electromagnetic field of a heavy nucleus is very short, $\sim 10^{-25}$ s, so that the photons in the resulting pulse are temporally coherent. Such a coherence might well give rise to an enhanced multiphoton contribution to the cross-section. The harder photon spectrum observed for sulphur interactions and the plethora of complex final states observed, especially in the sulphur sample, would also find a ready explanation in terms of multiphoton absorption.

7. CONCLUSIONS

This study has confirmed the results of Ardito et al. [12] that electromagnetic dissociation processes contribute significantly to the total nuclear inelastic cross-section of ultrarelativistic heavy ions passing through photographic emulsion. At 200 GeV per nucleon the pure EMD cross-section due to the visible channels is at the level of 12% of the pure nuclear cross-section for ^{16}O and 22% for ^{32}S. These results are in excellent agreement with those of other heavy-ion experiments, which employ completely different techniques and infer only indirectly the extent of EMD processes from the observed increase in the charge-changing cross-section with increasing energy of the particle.

There are obvious shortcomings in our experiment in that neutrons are rarely detected, isotopes are not separated, only the components of the momentum transverse to the beam

direction may be estimated, and events showing pion production are either eliminated from the sample by the scanning criteria or are misclassified as hadronic in origin. Nevertheless the use of high-energy ions as targets for a flux of comparatively low energy photons does allow the simultaneous study of a large number of different photoreactions on a given nuclear species. Such studies are difficult in direct photoproduction experiments.

The scanning procedure adopted has ensured that the detection efficiency for EMD events is very high and the contamination of the sample by hadronic interaction events is small, at least for photon energies up to the pion-production threshold. In fact it may well be that some of the 'small' events used to deduce the hadronic background could themselves arise from simultaneous electromagnetic dissociations of target and projectile nuclei.

Both the total and the various individual integrated cross-sections have been derived from our data by using the estimated energy release in each interaction and adopting the virtual photon spectrum computed according to the Weizsäcker–Williams formalism. These have been compared with the results, where available, from direct photodisintegration or photon emission experiments. There is good agreement with the directly measured (γ,p) cross-sections, especially in the region of the giant dipole resonance. The situation with respect to the total integrated cross-section measurement is, however, far less clear. After due allowance has been made for (γ,n) processes not observed in this experiment, there is a reasonable accord with the results of Ahrens et al. [29] for ^{16}O. However, our values are some 40% greater than the reassessed values up to photon energies of 40 MeV presented in the review of γ-^{16}O by Fuller [33]. Our cross-sections for the reactions (γ, α) in both oxygen and sulphur are much larger than those obtained by direct photon experiments. Contributions to our data, arising either from misidentified interactions such as (γ,^{3}He) or $(\gamma, \alpha n)$, or from an enhanced effect due to virtual photons with E2 multipolarity, do not explain the large discrepancy found. Another possibility, that some of the events assigned to the (γ,pp) channel are in reality (γ,tp), while similar numbers of so-called (γ, α) events are due to the charge-symmetric (γ,^{3}He n) reaction, cannot be tested in the present experiment.

There remain many final states for which the photon energies are above 50 MeV but there are no results from real photon experiments with which they may be compared.

Multiphoton processes were suggested by Ardito et al. [12] as a possible explanation of the complex break-ups of oxygen nuclei observed in that experiment. While the question of the presence or otherwise of an appreciable contribution from higher-order electromagnetic processes remains unresolved in this study, it could be answered in our future experiment, EMU09 [50], designed to observe EMD reactions from a va riety of foil targets with widely different atomic numbers.

It is a pleasure to acknowledge the excellent performance of the CERN Proton Synchrotron and Super Proton Synchrotron machines, and the enthusiastic work of the related personnel.

We are very grateful to our scanning teams for their patience and efficiency in finding and measuring such unusual events.

Support from the Mitsubishi Foundation, from the Japan Society for the Promotion of Science, and from the Monbusho International Scientific Research Program is greatly appreciated.

REFERENCES

[1] C.P. Powell, P.H. Fowler and D.H. Perkins, The study of elementary particles by the photographic method (Pergamon Press, London, 1959), p. 612.

[2] K. Rybicki, Nuovo Cimento **49** (1967) 203.

[3] H.H. Heckman and P.J. Lindstrom, Phys. Rev. Lett. **37**(1976) 56.

[4] G.D. Westfall et al., Phys. Rev. **C19** (1979) 1309.

[5] D.L. Olson et al., Phys. Rev. **C24** (1981) 1529.

[6] C. Brechtmann, W. Heinrich and E.V. Benton, Phys. Rev. **C39** (1989) 222.

[7] M.T. Mercier et al., Phys. Rev. Lett. **52** (1984) 898.

[8] M.T. Mercier et al., Phys. Rev. **C33** (1986) 1655.

[9] J.C. Hill et al., Phys. Rev. Lett. **60** (1988) 999.

[10] J.C. Hill et al., Phys. Rev. **C38** (1988) 1722.

[11] J.C. Hill et al., Phys. Rev. **C39** (1989) 524.

[12] N. Ardito et al., Europhys. Lett. **6** (1988) 131.

[13] C. Brechtmann and W. Heinrich, Z. Phys. **A330** (1988) 407.

[14] C. Brechtmann and W. Heinrich, Z. Phys. **A331** (1988) 463.

[15] B.P. Price et al., Phys. Rev. Lett. **61** (1988) 2193.

[16] C.F. von Weizsäcker, Z. Phys. **88** (1934) 612.
E.J. Williams, Phys. Rev. **45** (1934) 729.

[17] J.D. Jackson, *in* Classical electrodynamics, 2nd ed. (Wiley and Sons, Inc., New York, 1975).

[18] J.S. Levinger, Phys. Rev. **84** (1951) 43; Phys. Lett. **B82** (1979) 181.

[19] W.H. Barkas, Nuclear research emulsions, Vol. I (Academic Press, Inc., New York, 1963).

[20] G. Baroni et al., in preparation.

[21] E.M. Friedlander et al., Phys. Rev. **C27** (1983) 1489.

[22] G. Baroni et al., in preparation.

[23] B. Rossi, *in* High-energy particles (Prentice Hall, Englewood Cliffs, NJ, 1952).

[24] C.A. Bertulani and G. Baur, Phys. Rep. **163** (1988) 299.

[25] J.H. Derrickson et al., NASA TM-100347 (1988).

[26] M.I. Adamovich et al., Phys. Rev. **C40** (1989) 66.

[27] P.M. Endt and C. Van der Leun, Nucl. Phys. **A310** (1978) 1.

[28] E. Andersen et al., Phys. Lett. **B220** (1989) 328.

[29] J. Ahrens et al., Nucl. Phys. **A251** (1975) 479.

[30] A.N. Gorbunov and V.A. Osipova, Sov. Phys.–JETP **16** (1963) 27.
A.N. Gorbunov et al., Sov. Phys.–JETP **15** (1962) 520.

[31] A. Veyssière et al., Nucl. Phys. **A227** (1974) 513.

[32] J.T. Caldwell et al., Phys. Rev. Lett. **19** (1967) 447.

[33] E.G. Fuller, Phys. Rep. **127** (1985) 185.

[34] P.J. Carlos, Lecture Notes in Physics **137** (1981) 168.

[35] V.M. Maikov, Sov. Phys.–JETP **7** (1958) 973.
[36] M.E. Toms, Nucl. Phys. **54** (1964) 625.
[37] K. Kramer et al., Z. Phys. **207** (1967) 1.
[38] R. Jäckle and H. Pilkuhn, Nucl. Phys. **A247** (1975) 521.
[39] A. Winther and K. Alder, Nucl. Phys. **A319** (1979) 518.
[40] A. Goldberg, Nucl. Phys. **A420** (1984) 636.
[41] B. Hoffmann and G. Baur, Phys. Rev. **C30** (1984) 247.
[42] C.A. Bertulani and G. Baur, Nucl. Phys **A442** (1985) 739.
[43] M.N. Martins et al., Phys. Rev. **C26** (1982) 1936.
[44] J.M. Wyckoff et al., Phys. Rev. **137** (1965) B576.
[45] D.W. Anderson et al., Nucl. Phys. **A156** (1970) 74.
[46] G. Bonazzola et al., Nucl. Phys. **34** (1962) 637.
[47] B.S. Dolbilkin et al., Sov. J. Nucl. Phys. **8** (1969) 626.
[48] L. Meyer-Schützmeister et al., Nucl. Phys. **A108** (1968) 180.
[49] G. Baur and C.A. Bertulani, Phys. Lett. **B174** (1986) 23.
[50] N. Armenise et al. (EMU09 Collab.), proposal CERN/SPSC/89–1, P–243 (1989).

Table 1

Global data on the interactions of primary (^{16}O and ^{32}S) and secondary (He to N) 200 GeV/N projectiles in nuclear emulsion

Nucleus	Tracks	L (m)	N_{nuc}	λ_{nuc} (mm)	N_{EMD}	λ_{EMD} (mm)
^{16}O	13375	348.7	2934	119 ± 2	362	960 ± 50
^{32}S	8068	198.5	2168	92 ± 2	476	420 ± 20
He	1559	75.9	335	226 ± 12	13	5800 ± 1600
Li	120	5.7	32	178 ± 31	2	2800 ± 2000
Be	109	4.7	32	146 ± 26	6	780 ± 320
B	142	6.1	48	128 ± 18	3	2000 ± 1200
C	292	13.3	86	154 ± 17	11	1200 ± 360
N	326	13.4	110	122 ± 12	8	1700 ± 600

Table 2

Numbers and relative rates of visible channels from 200 GeV/N ^{16}O and ^{32}S electromagnetic dissociation. Isotopes not separated. Energies computed as shown in subsection 3.3.

	Energy (MeV)			Fraction (%)		Energy (MeV)			Fraction (%)
$^{16}O \rightarrow$	0–150	>150	(>500)		$^{32}S \rightarrow$	0–150	>150	(>500)	
NH	196	6	(1)	56 ± 4	PH	251	5	-	54 ± 3
C2H	48	4	(1)	14 ± 2	Si2H	104	8	-	24 ± 2
CHe	36	-	-	10 ± 2	SiHe	27	-	-	6 ± 1
BHeH	13	-	-	4.4	AlHeH	15	3	-	6.7
B3H	2	1	-		Al3H	10	4	(2)	
Be ...	13	5	(2)	4.7	Mg ...	9	9	(3)	3.8
Li ...	5	4	-	2.5	Na ... Ne ... F ...	5	10	(5)	3.2
4He	3	-	-	8.0					3.4
3He2H	9	5	(2)		O ...				
2He4H	1	9	(2)		. ...	7	9	(6)	
He6H	-	2	(1)		He...				
TOTAL	326	36	(9)		TOTAL	428	48	(16)	

Note: two He isotopes with separation angle $\Delta\theta < 0.1$ mrad are considered as a ^{8}Be nucleus.

Table 3

Evaluation of the numbers of spurious events
from peripheral strong nuclear interactions simulating projectile EMDs

Sample	Oxygen		Sulphur	
	Total	Analysed	Total	Analysed
Nuclear interactions	2934	920	2168	609
EMDs	362	112	476	124
$n_H > 0$, all $\theta < 5$ mrad		7		6
$n_H > 0$, $n_s = 6 - 10$[a)]	317		181	
$n_H = 0$, $n_s = 6 - 10$[a)]	229		149	
Nuclear interactions simulating EMD	$7 \times (2934/920)\,(229/317) = 16 \pm 6$		$6 \times (2168/609)\,(149/181) = 18 \pm 7$	

a) $n_s = 6 - 12$ for the sulphur sample.

Table 4

Characteristics of events simulating projectile EMDs

Channel	$n_H > 0$, $n_s \leq 6$ outside $\theta = 5$ mrad									
	Oxygen					Sulphur				
	Energy (MeV)					Energy (MeV)				
	Tot.	0–150	>150	(>500)	Fract. (%)	Tot.	0–150	>150	(>500)	Fract. (%)
f	16	Not measurable				9	Not measurable			
fH	15	9	6	(1)	24	9	5	4	(1)	28
fHH	17	7	10	(7)	27	8	3	5	(4)	25
fHe	2	2	–	–	3	1	1	–	–	3
fHeH	3	2	1	(1)	5	–	–	–	–	–
f3H	6	2	4	(3)	10	6	3	3	(2)	19
Others	19	11	8	(4)	31	8	1	7	(5)	25
Total	78					41				

Table 5
Computed numbers of spurious events
due to nuclear interactions in the EMD samples

Channel	Oxygen			Sulphur		
	Energy (MeV)			Energy (MeV)		
	0–150	>150	(>500)	0–150	>150	(>500)
fH	2.3	1.5	(0.3)	2.8	2.2	(0.6)
fHH	1.8	2.6	(1.8)	1.7	2.8	(2.2)
fHe	0.5	–	–	0.5	–	–
fHeH	0.5	0.3	(0.3)	–	–	–
f3H	0.5	1.1	(0.8)	1.7	1.7	(1.1)
Others	2.9	2.0	(1.0)	0.6	4.0	(2.9
Total	8.5	7.5	(4.2)	7.3	10.7	(6.8)

Table 6
Raw and corrected data for projectile EMD events with E < 150 MeV

Events		Lost		Gained		Total corrected data
Channel	Raw data	Nuclear interac.	EMD misid.	EMD misid.	Nuclear periph.	
Oxygen →						
NH	196	4.7	0.4	1.7	2.3	197.1
C2H	48	0.8	1.4	0.3	1.8	48.1
CHe	36	1.6	0.2	0.1	0.5	37.2
BHeH	13	0.4	0.6	0.1	0.5	13.4
B3H	2	0.1	0.1	0.1	0.5	1.7
Others	31	1.0	0.5	0.5	2.9	29.1
Total	326	11.8		11.3		326.5
Sulphur →						
PH	251	13.7	1.9	5.9	2.8	257.9 + 24[a]
Si2H	104	4.9	6.0	1.5	1.7	111.7
SiHe	27	2.8	0.4	0.1	0.5	29.6
AlHeH	15	0.7	1.4	0.3	–	16.8
Al3H	10	0.7	0.8	1.1	1.7	8.7
Others	21	1.5	1.0	1.6	0.6	21.3
Total	428	35.8		17.8		446.0 + 24

a) From scanning losses.

Table 7

Separation energies (B) for some combinations of fragments from ^{16}O and ^{32}S. Heaviest fragment not shown when $Z \geq 3$.

Reaction products	B (MeV)	
	Oxygen	Sulphur
n	15.6	15.0
nn	28.9	28.1
p	12.1	8.9
pn	23.0	21.2
pp	22.3	16.1
ppn	30.5	26.8
^{3}He	22.8	19.1
α	7.2	6.9
αn	25.9	24.1
αp	23.1	18.5
αpn	34.6	31.6
3p3n	62.9	59.9
α2p2n	42.8	45.2
4p4n	71.1	73.5
2αpn	39.0	38.6
α3p3n	67.3	69.3
$^{16}O \rightarrow 4\alpha$	14.4	
3α2p2n	42.7	
2α4p4n	71.0	
$^{32}S \rightarrow {}^{22}Na{}^{6}Li2p2n$		70.8
$^{20}Ne2\alpha2p2n$		54.5

Table 8

Observed inverse slopes (T) of the energy distributions for different channels compared with the separation energy (B) of the fragments. Fits to distributions of the form exp (– E/T) were performed up to E_t. T_0 is the value of T corrected for the c.m. angular distribution.

	E_t (MeV)	T (MeV)	T_0 (MeV)	T_0/B
O → Np	40	10.5 ± 1.0	9.4 ± 0.9	0.77 ± 0.07
Cα	150	9.6 ± 1.6	8.6 ± 1.4	1.19 ± 0.19
Cpp	70	25 ± 6	17 ± 4	0.75 ± 0.18
Bαp	70	10 ± 3	7 ± 2	0.29 ± 0.09
S → Pp	40	8.4 ± 0.6	7.5 ± 0.5	0.85 ± 0.06
Siα	150	8.3 ± 1.6	7.4 ± 1.4	1.07 ± 0.20
Sipp	70	21 ± 3	14 ± 2	0.87 ± 0.12
Alαpn	120	45 ± 20	30 ± 13	0.95 ± 0.41

Table 9

200 GeV/N oxygen-silver and sulphur-silver pure nuclear and projectile EMD cross-sections obtained in the present experiment and in other experiments; $\sigma(\Delta Z > 0)$ is the charge-changing cross-section.

	λ (cm)[a]	f[b]	σ (mb)	$\sigma(\Delta Z > 0)$ (mb)	References
Pure nuclear interactions					
O-Emulsion	11.9 ± 0.2	0.29	2620 ± 50		This exp.
O-Ag			2506 ± 47	2411 ± 63	[13]
S-Emulsion	9.2 ± 0.2	0.26	3100 ± 70		This exp.
S-Ag				2935 ± 100	[14]
S-Ag				3040 ± 120	[27]
Projectile EMDs					
O-Em. (E < 150)	107 ± 6	0.61		615 ± 35	This exp.
O-Em. (No cut)	98 ± 5	0.61		670 ± 35	
O-Ag				652 ± 60	[13]
S-Em. (E < 150)	42 ± 2	0.61		1560 ± 80	This exp.
S-Em. (No cut)	39 ± 2	0.61		1680 ± 80	
S-Ag				1790 ± 120	[14]
S-Ag				1380 ± 190	[27]

a) Interaction length.

b) Estimated fraction of events with a silver target.

Table 10

Projectile EMD partial cross-sections (in mb) for the production of fragments, with charge Z_F as the heaviest fragment, from 200 GeV/N ^{16}O and ^{32}S ions on silver

Z_F =	7	6	5	4	3	2	≤ 5	Ref.
O-Emul. (E < 150)	371 ± 26	161 ± 17	28 ± 7	24 ± 7	9 ± 4	23 ± 7	83 ± 13	This experiment
O-Emul. (No cut)	380 ± 27	163 ± 18	28 ± 7	32 ± 8	17 ± 6	49 ± 10	126 ± 15	
O-Ag	342 ± 22	127 ± 21					183 ± 50	[13]
Z_F =	15	14	13	12	11 + 10	9 + 8	≤ 7	
S-Emul. (E < 150)	933 ± 57	468 ± 40	84 ± 17	30 ± 10	10 ± 6	20 ± 8	10 ± 6	This experiment
S-Emul. (No cut)	942 ± 58	485 ± 42	102 ± 20	60 ± 15	30 ± 10	33 ± 11	26 ± 9	
S-Ag	832 ± 16	413 ± 15	94 ± 10	86 ± 8	83 ± 8	51 ± 6		[14][a]

a) Results computed from factorization formulae and an arbitrary normalization: see text.

Table 11

Integrated photonuclear cross-sections deduced from oxygen EMD and compared with real photon cross-sections. The errors are purely statistical.

$$\sigma_{int}(E) = \int_0^E \sigma(E_\gamma)\, dE_\gamma \quad (MeV \cdot mb)$$

E (MeV)	(γ,p)	(γ,pp)	Others	Total charged	$(\gamma,abs)^{a)}$	$(\gamma,n)^{b-d)}$	$(\gamma,p)^{b,d,e)}$	$(\gamma,np)^{b,c)}$
10			2	2				
15	23 ± 3		7 ± 2	30 ± 4	10			
20	55		10	65	32			
25	84	2	16	102	135	27	85	
30	110 ± 9	12 ± 3	22 ± 4	144 ± 10	210	50	95	5
35	125	21	32	178	255	60		10
40	139	25	34	198	290	70	100	
50	152 ± 12	37 ± 7	42 ± 7	231 ± 15	330	75	105	
60	155	44	47	246	360	80		
80	163	70	70	303	410	80	107	
100	163 ± 13	75 ± 13	99 ± 16	337 ± 25	432			
140	169 ± 14	119 ± 21	163 ± 26	451 ± 36	508			

a) J. Ahrens et al., Nucl. Phys. **A251** (1975) 479.
b) A.N. Gorbunov and V.A. Osipova, Sov. Phys.-JETP **16** (1963) 27.
c) A. Veyssière et al., Nucl. Phys. **A227** (1974) 513.
d) E.G. Fuller, Phys. Rep. **127** (1985) 185.
e) J.T. Caldwell et al., Phys. Rev. Lett. **19** (1967) 447.

Table 12

Integrated photonuclear cross-sections deduced from sulphur EMD and compared with real photon cross-sections. The errors are purely statistical.

$$\sigma_{int}(E) = \int_0^E \sigma(E_\gamma)\, dE_\gamma \quad (MeV \cdot mb)$$

E (MeV)	(γ,p)	(γ,pp)	Others	Total charged	(γ,abs)[a,b]	(γ,n)[c]	(γ,p)[d]	(γ, np)[c,e]
10	7		5	12				
15	100 ± 9		10 ± 3	110 ± 10	12		75	
20	173	10	16	210	140	32		
25	206	44	26	276	310	84		
30	234 ± 16	92 ± 12	28 ± 6	354 ± 21	400	107	275	24
35	270	114	28	412	470	123		35
40	281	134	32	447	525[f]	131		46
50	293 ± 20	178 ± 20	36 ± 8	507 ± 30	600[f]	145		57
60	305	191	36	532	650[f]	155		64
80	327	253	92	672	730[f]			71
100	335 ± 26	284 ± 32	166 ± 32	785 ± 52	790[f]			
140	374 ± 34	322 ± 39	286 ± 50	982 ± 71	940[f]			

a) J.M. Wyckoff et al., Phys. Rev. **137** (1965) B576.
b) J. Ahrens et al., Nucl. Phys. **A251** (1975) 479.
c) D.W. Anderson et al., Nucl. Phys. **A156** (1970) 74.
d) B.S. Dolbilkin et al., Sov. J. Nucl. Phys. **8** (1969) 626.
e) G. Bonazzola et al., Nucl. Phys. **34** (1962) 637.
f) Interpolated from data on Al and Ca in ref. (b) above.

Figure captions

Fig. 1: Diagram of projectile electromagnetic dissociation (EMD).

Fig. 2: The energy spectrum of virtual photons for 200 GeV/nucleon ^{16}O projectiles in nuclear emulsion.

Fig. 3: Microphotograph of a complex projectile EMD (200 GeV/N ^{32}S).

Fig. 4: Microphotograph of a possible target EMD (200 GeV/N ^{16}O).

Fig. 5: Distribution of projectile EMD events as a function of the along-the-beam coordinate for both oxygen and sulphur samples.

Fig. 6: Nuclear interaction (o) and projectile EMD (x) mean free paths in nuclear emulsion as a function of projectile charge at 200 GeV/N.

Fig. 7: Plots of the vertical ($\Delta\delta$) versus the horizontal ($\Delta\alpha$) component of the relative separation angles between the $Z = 1$ track and the fragment in the dissociation O $\rightarrow$ NH (a) and S $\rightarrow$ PH (b), both at 200 GeV/N.

Fig. 8: Charge distribution, from δ-ray density, of a sample of secondary projectile fragments from 200 GeV/N ^{16}O-emulsion interactions.

Fig. 9: Charge distribution, from δ-ray gaps, of a sample of primaries and of fragments from projectile EMDs (200 GeV/N ^{32}S on emulsion). Solid line: expected shape, normalized to $Z = 14$. Dotted line: $Z = 15$, not measured in this sample.

Fig. 10: Energy spectra for different channels observed in the sample of 200 GeV/N oxygen EMDs.

Fig. 11: Sketch of the most likely contributions to losses or biases of EMD events due to close interactions. An asterisk (*) represents a nuclear interaction; an arrow ($\uparrow$) represents a projectile EMD.

Fig. 12: Corrected energy spectra for different channels observed in the 200 GeV/N sulphur EMD. The shaded area shows the size of the corrections, only noticeable in the lower energy bins.

Fig. 13: Azimuthal angle φ between protons as a function of energy in the channels O $\rightarrow$ CHH (a) and S $\rightarrow$ SiHH (b).

Fig. 14: Energy spectra from events in the HH channels in ^{16}O (a) and ^{32}S (b) EMD obtained by neglecting one proton, compared with the original HH and with the true H spectra.

Fig. 15: Integrated energy spectra of the most abundant reactions in the EMD of 200 GeV/N oxygen projectiles. Exponentially decreasing shapes are clearly favoured.

Fig. 16: Integrated energy spectra of the most abundant reactions in the EMD of 200 GeV/N sulphur projectiles. Coulomb barrier effects that are stronger than in oxygen are possibly seen.

Fig. 17: Shape of two-body energy spectra reconstructed from transverse momenta with a monochromatic (E^*) spectrum in the c.m. system but different angular distributions of the outgoing fragments: E' is the 'transverse' energy; E is the total energy having assumed isotropy.

Fig. 18: a) Transformation of an exponentially decreasing energy spectrum in the c.m. system (full line) for different angular distributions and having assumed isotropy.

b) Normalized energy distribution of the O $\rightarrow$ Np sample compared with that transformed from eq. (11) and isotropic emission. Assuming that $T_0 = 9$ MeV (see text), the best agreement is found for $E_s = 1.5$ MeV.

Fig. 19: Single reactions (σ_γ) and total charged (σ_γ^{ch}) photoproduction cross-sections on oxygen deduced from EMD cross-sections and assuming a classical energy spectrum of virtual photons [eq. (3)].

Fig. 20: The same as in fig. 19, but for sulphur.

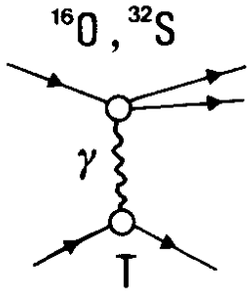
^{16}O , ^{32}S
γ
T

Fig. 1

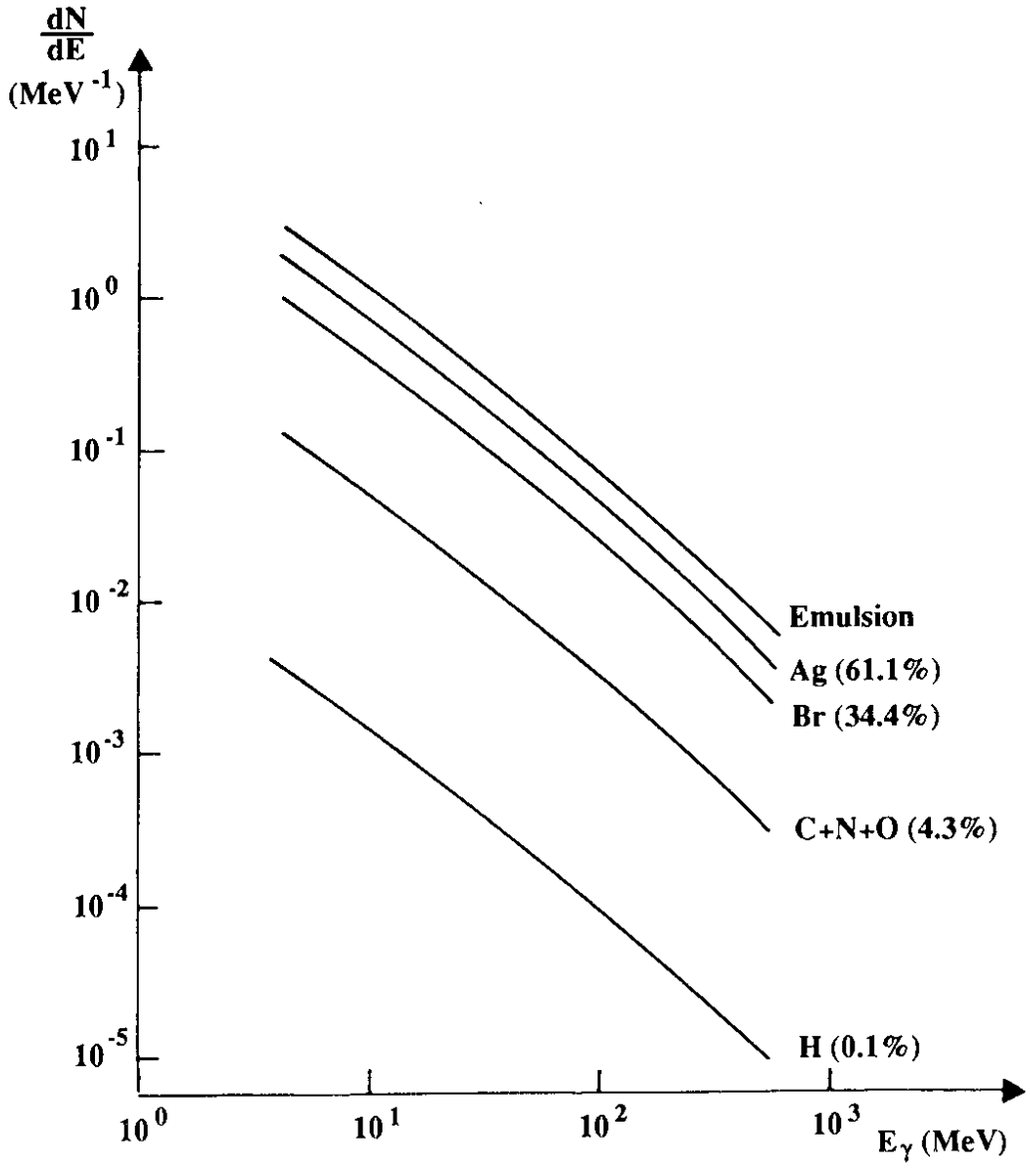
dN/dE
(MeV^{-1})
10^{1}
10^{0}
10^{-1}
10^{-2}
10^{-3}
10^{-4}
10^{-5}
Emulsion
Ag (61.1%)
Br (34.4%)
C+N+O (4.3%)
H (0.1%)
10^{0}
10^{1}
10^{2}
10^{3}
E_γ (MeV)

Fig. 2

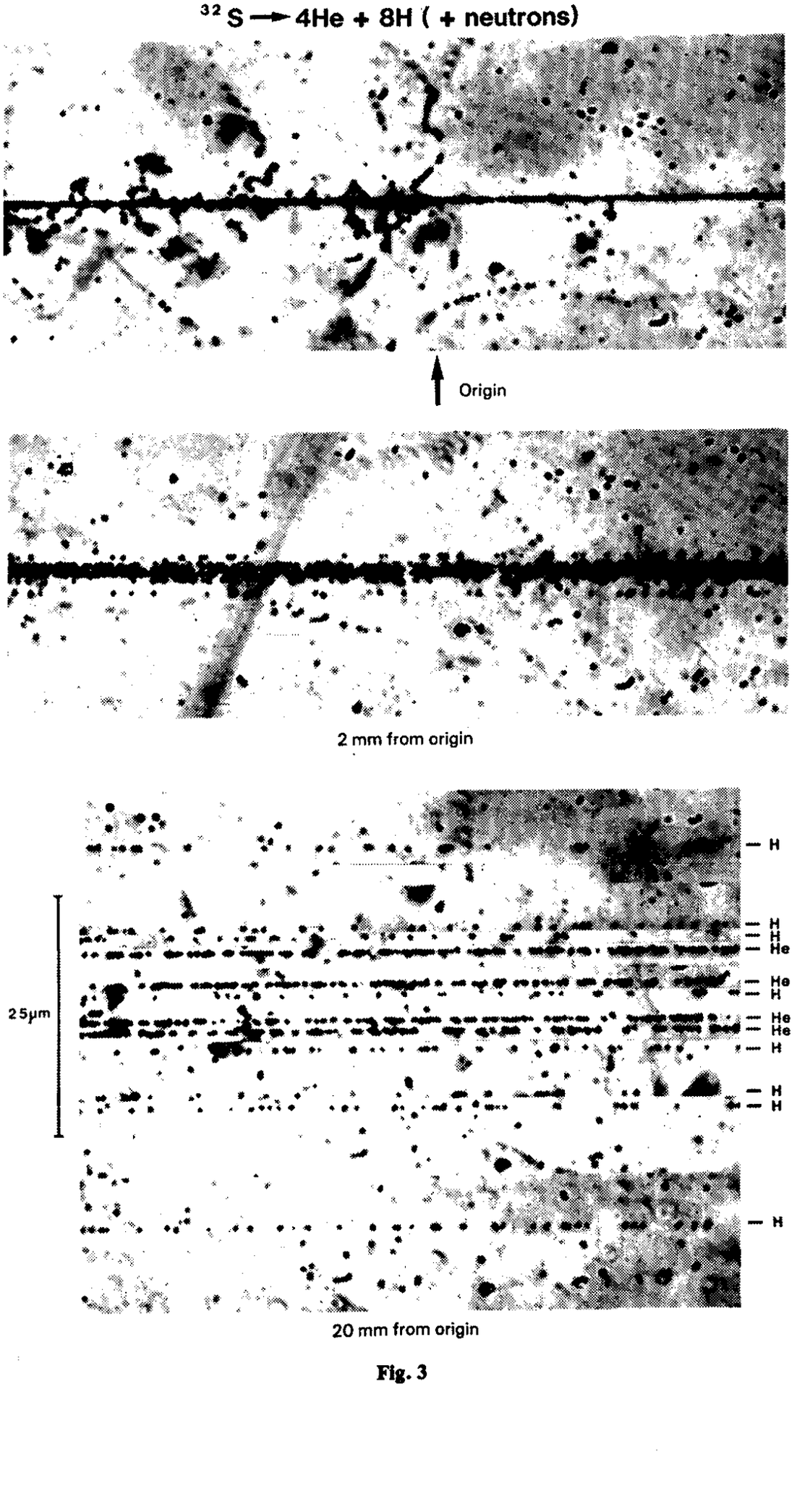
$^{32}S \rightarrow 4He + 8H$ (+ neutrons)
Origin
2 mm from origin
25μm
H
H
H
He
He
H
He
He
H
H
H
H
20 mm from origin

Fig. 3

$$^{16}O + ^{12}C \rightarrow ^{16}O + 3\,^{4}He$$

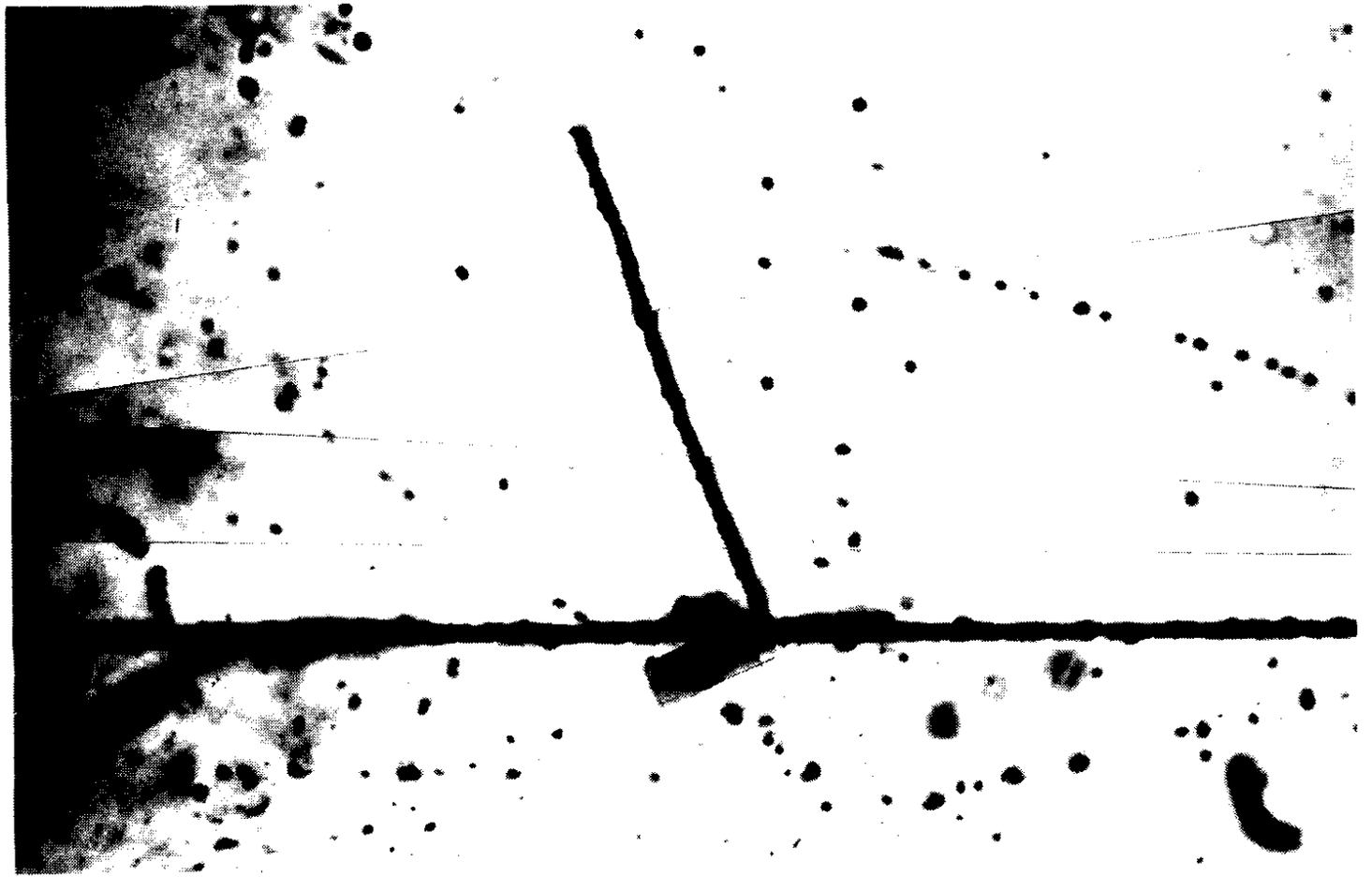

Fig. 4

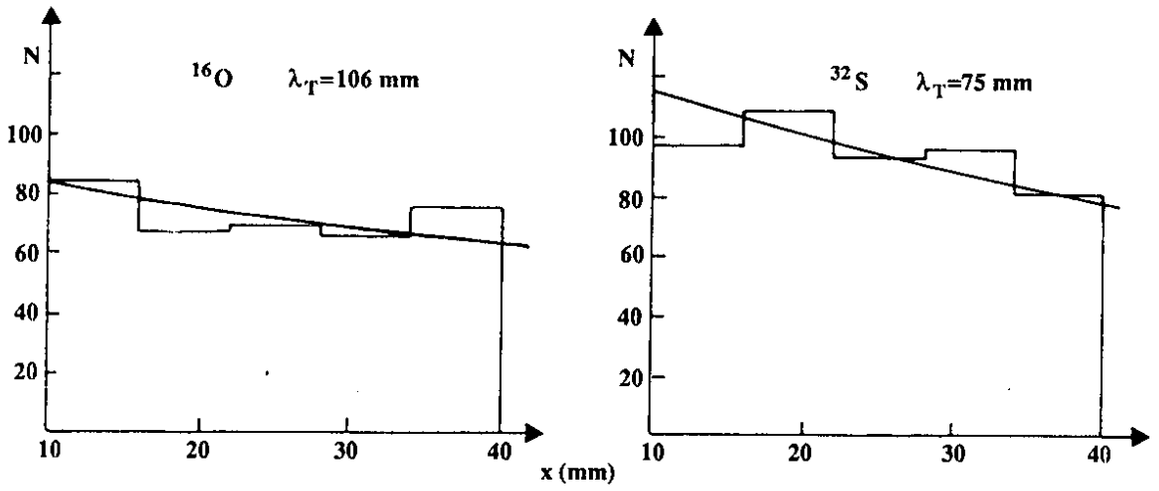
N
^{16}O
λ_T=106 mm
100
80
60
40
20
10
20
30
40
x (mm)
N
^{32}S
λ_T=75 mm
100
80
60
40
20
10
20
30
40

Fig. 5

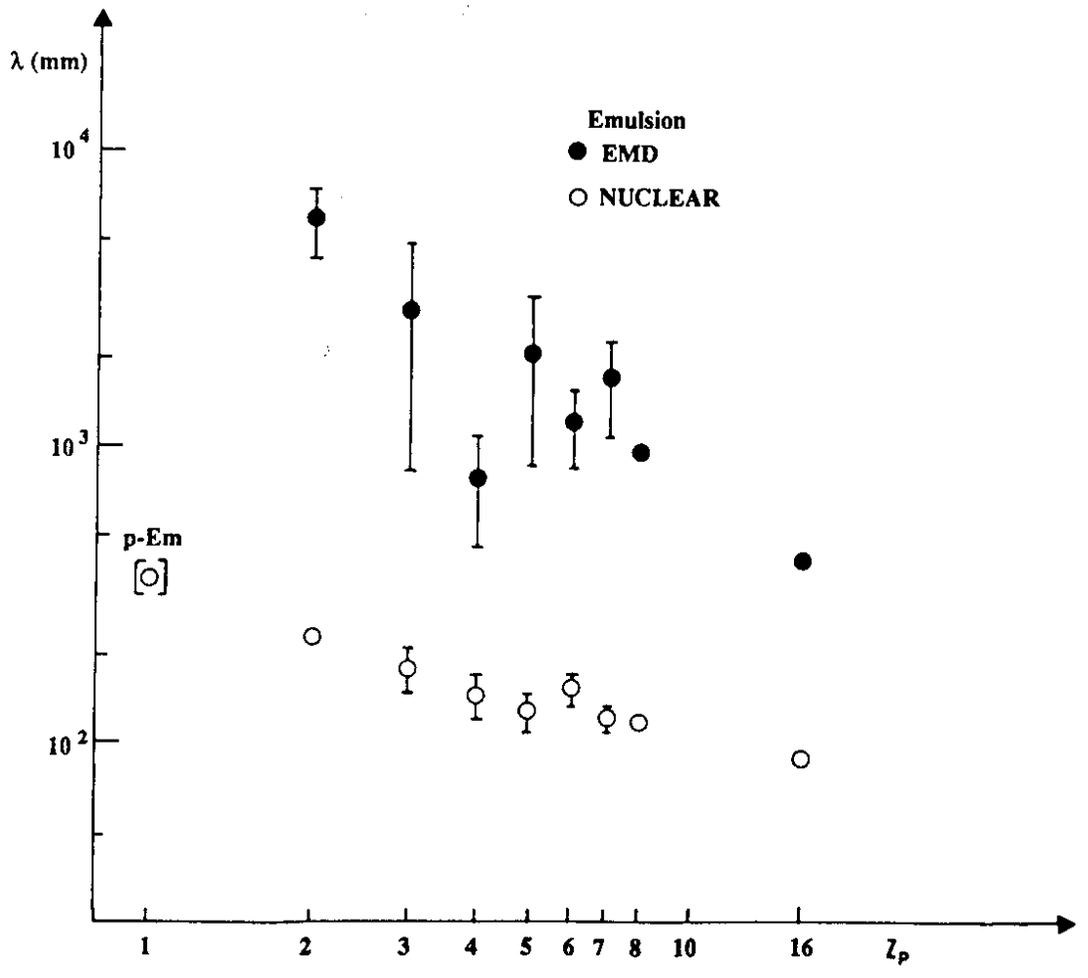
λ (mm)
10^4
10^3
10^2
Emulsion
EMD
NUCLEAR
p-Em
1
2
3
4
5
6
7
8
10
16
Z_P

Fig. 6

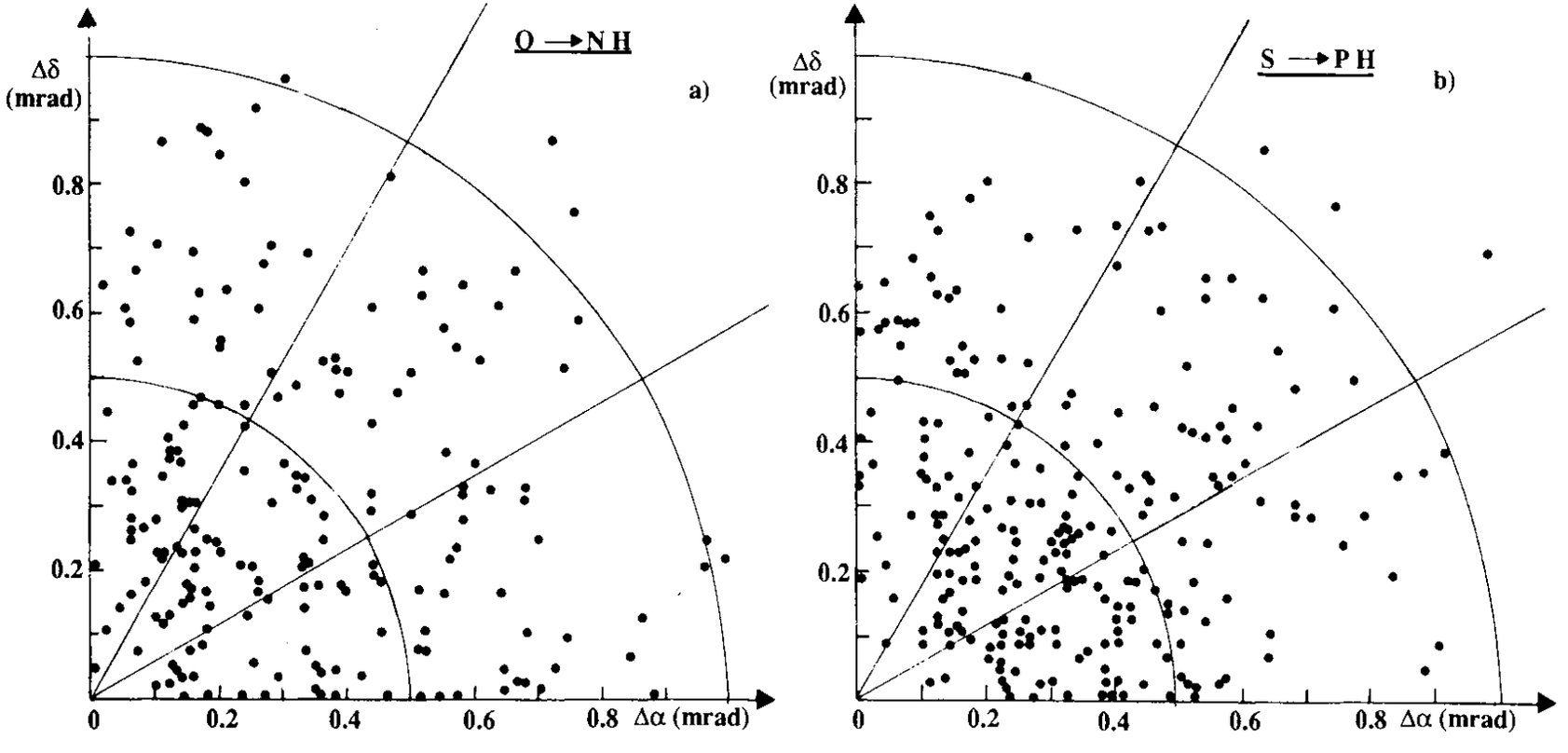
O → N H
a)
Δδ (mrad)
0.8
0.6
0.4
0.2
0
0.2
0.4
0.6
0.8
Δα (mrad)
S → P H
b)
Δδ (mrad)
0.8
0.6
0.4
0.2
0
0.2
0.4
0.6
0.8
Δα (mrad)

Fig. 7

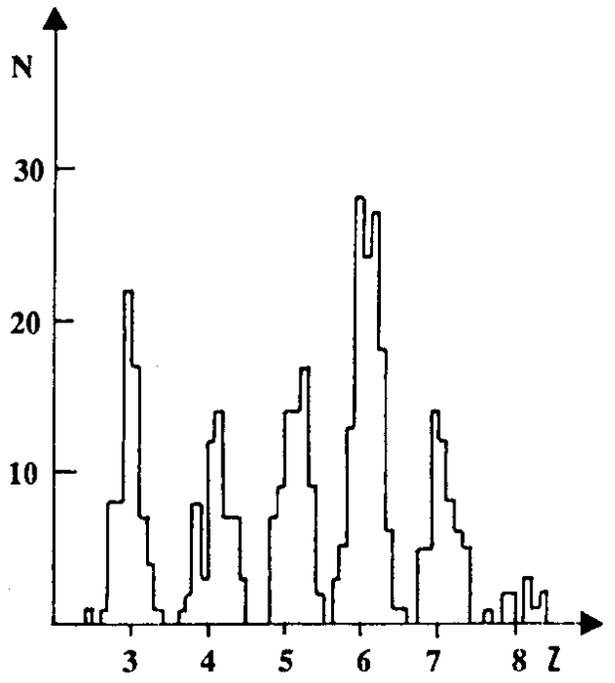

Fig. 8

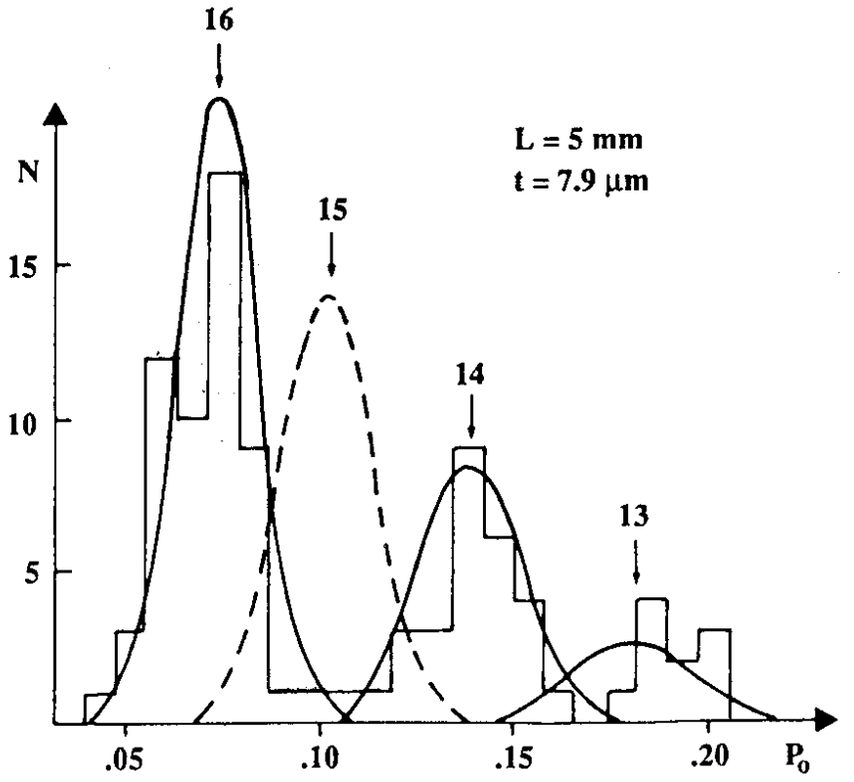

Fig. 9

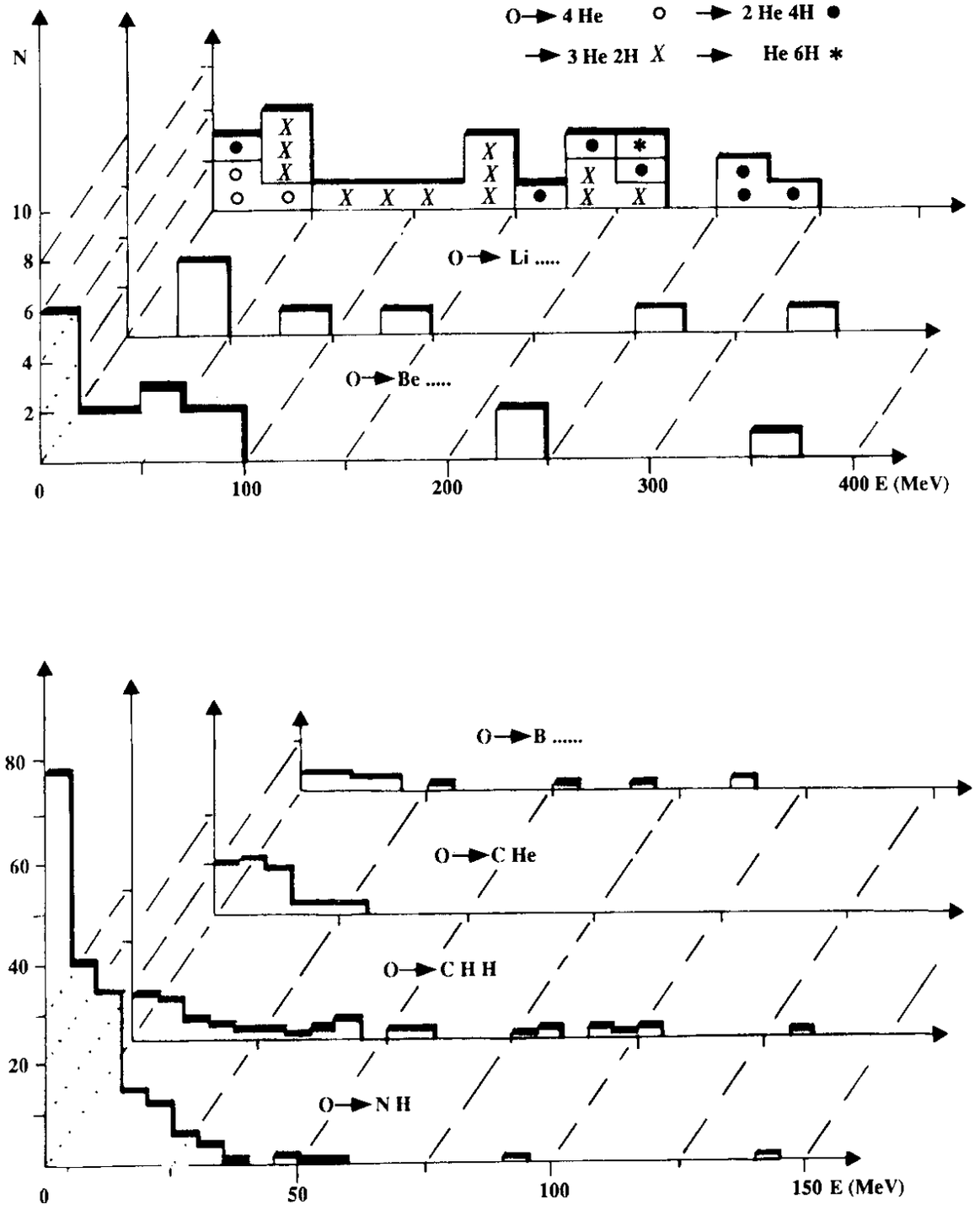
O→ 4 He
→ 2 He 4H
→ 3 He 2H
→ He 6H
N
10
8
6
4
2
O→ Li .....
O→ Be .....
0
100
200
300
400 E (MeV)
80
60
40
20
O→ B .....
O→ C He
O→ C H H
O→ N H
0
50
100
150 E (MeV)

Fig. 10

CHANNEL : S → P H

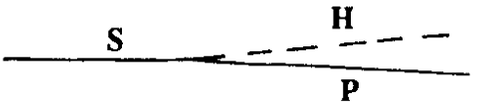

LOSSES

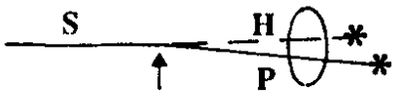

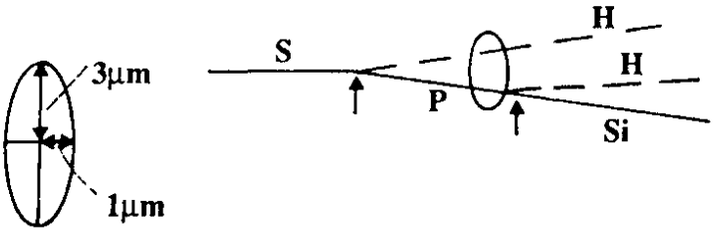

Assign.		Estim. n°
nucl. int.		13.7
EMD →	Si 2H	1.0
→	Al He H	0.1
→	Al 3H	0.5
→	...	0.3

GAINS

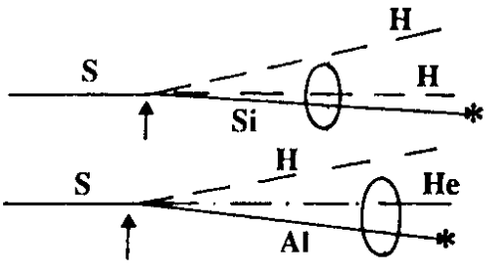

→	PH	
↳	*	4.8
→	PH	
↳	*	1.1

Fig. 11

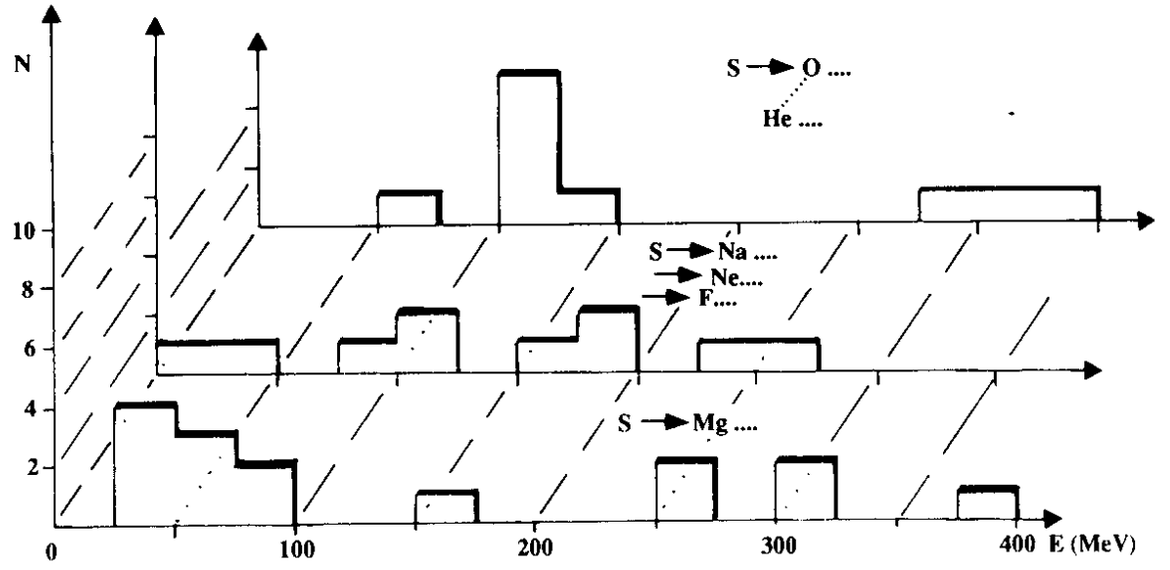
N
S → O ....
He ....
10
8
6
4
2
S → Na ....
→ Ne....
→ F....
S → Mg ....
0
100
200
300
400 E (MeV)

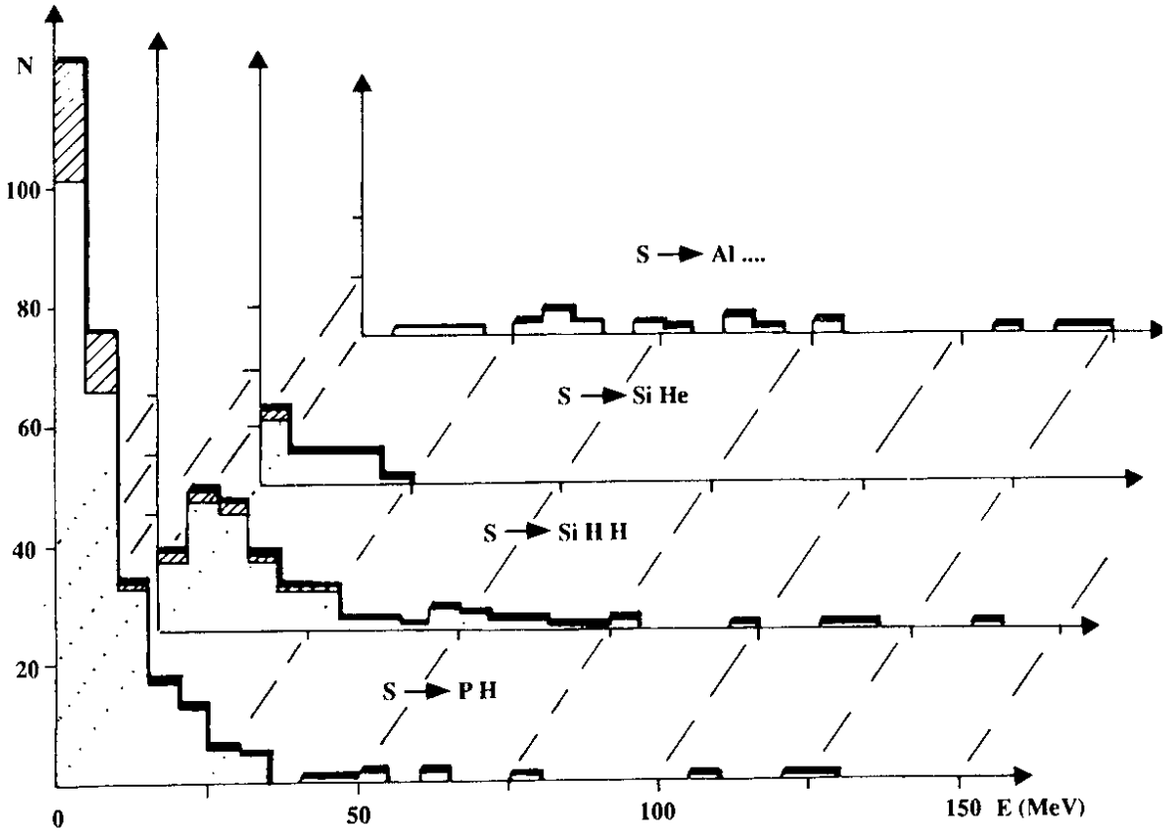
N
100
80
60
40
20
S → Al ....
S → Si He
S → Si H H
S → P H
0
50
100
150 E (MeV)

Fig. 12

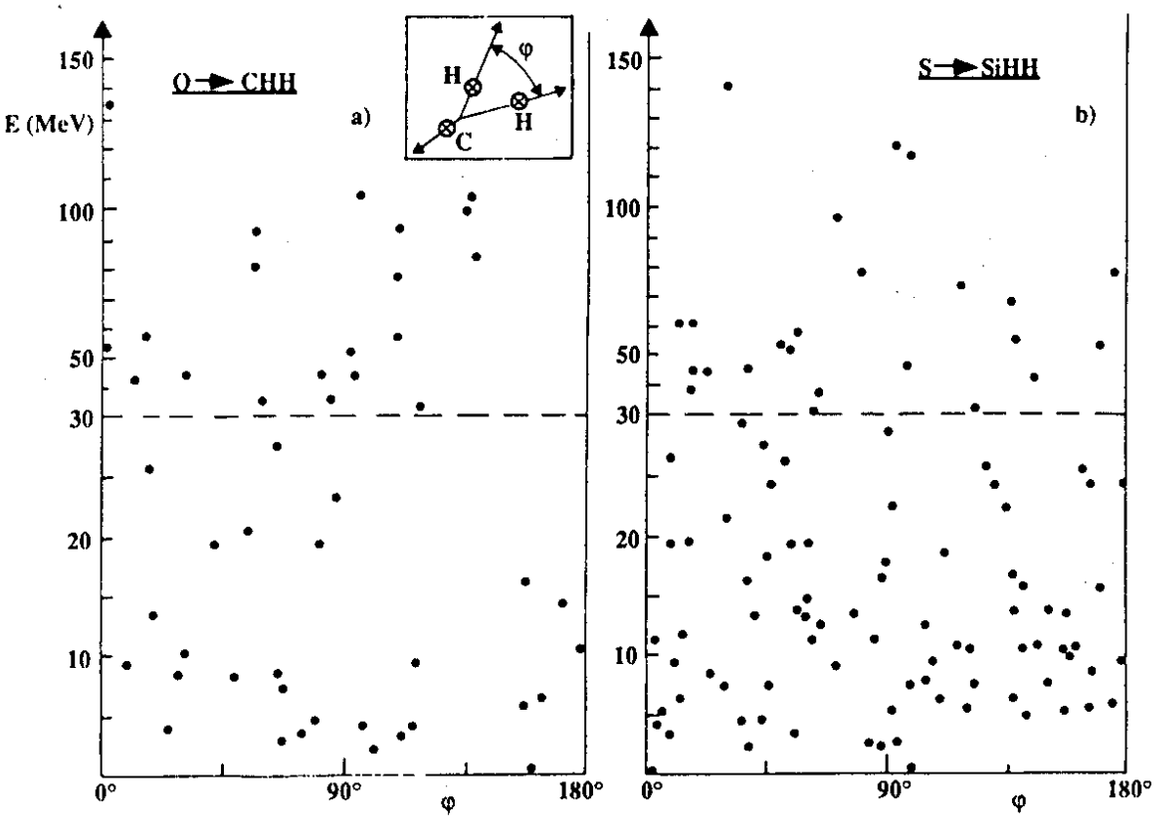

Fig. 13

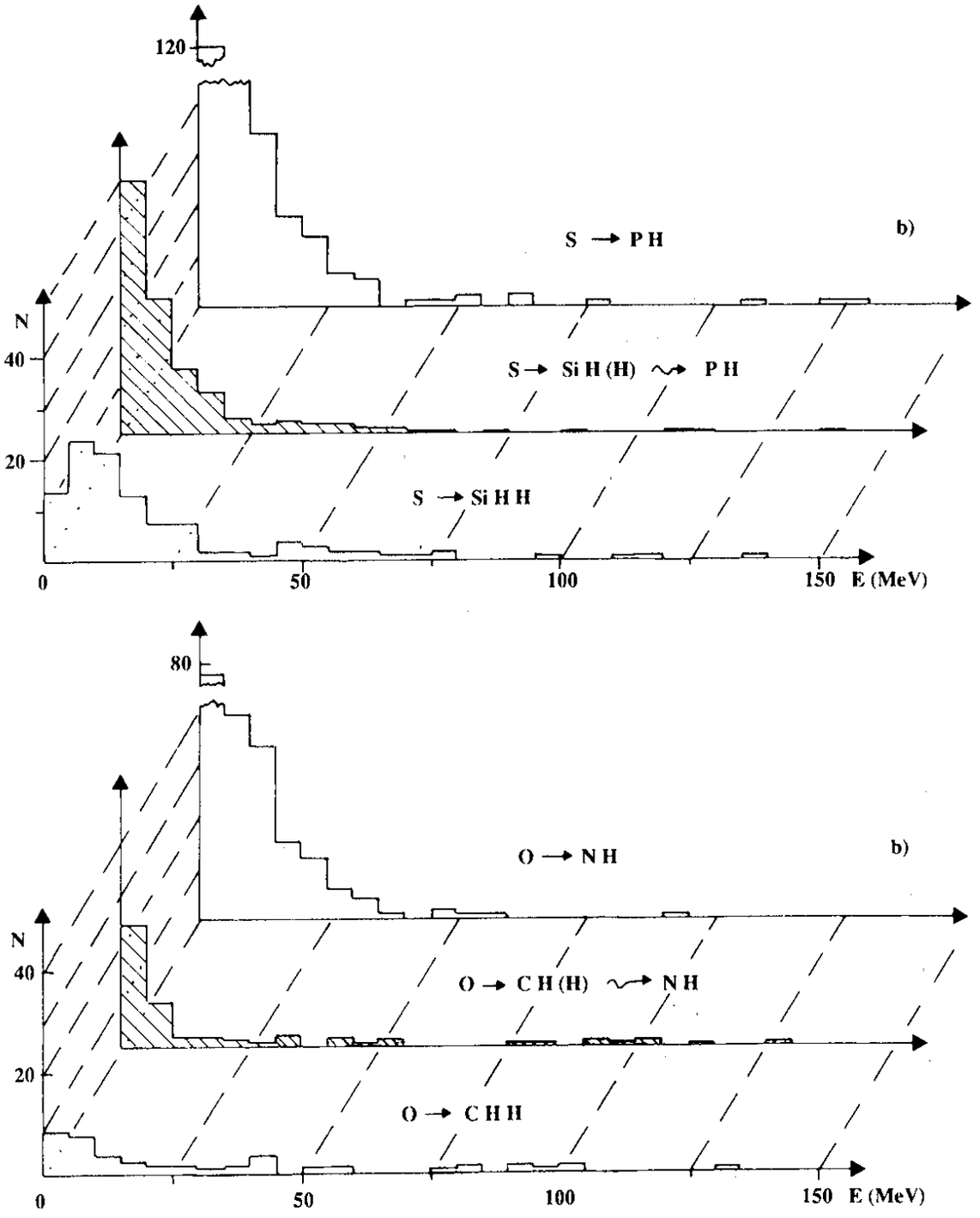
120
N
40
20
S → P H
b)
S → Si H (H) ⇝ P H
S → Si H H
0
50
100
150
E (MeV)
80
N
40
20
O → N H
b)
O → C H (H) ⇝ N H
O → C H H
0
50
100
150
E (MeV)

Fig. 14

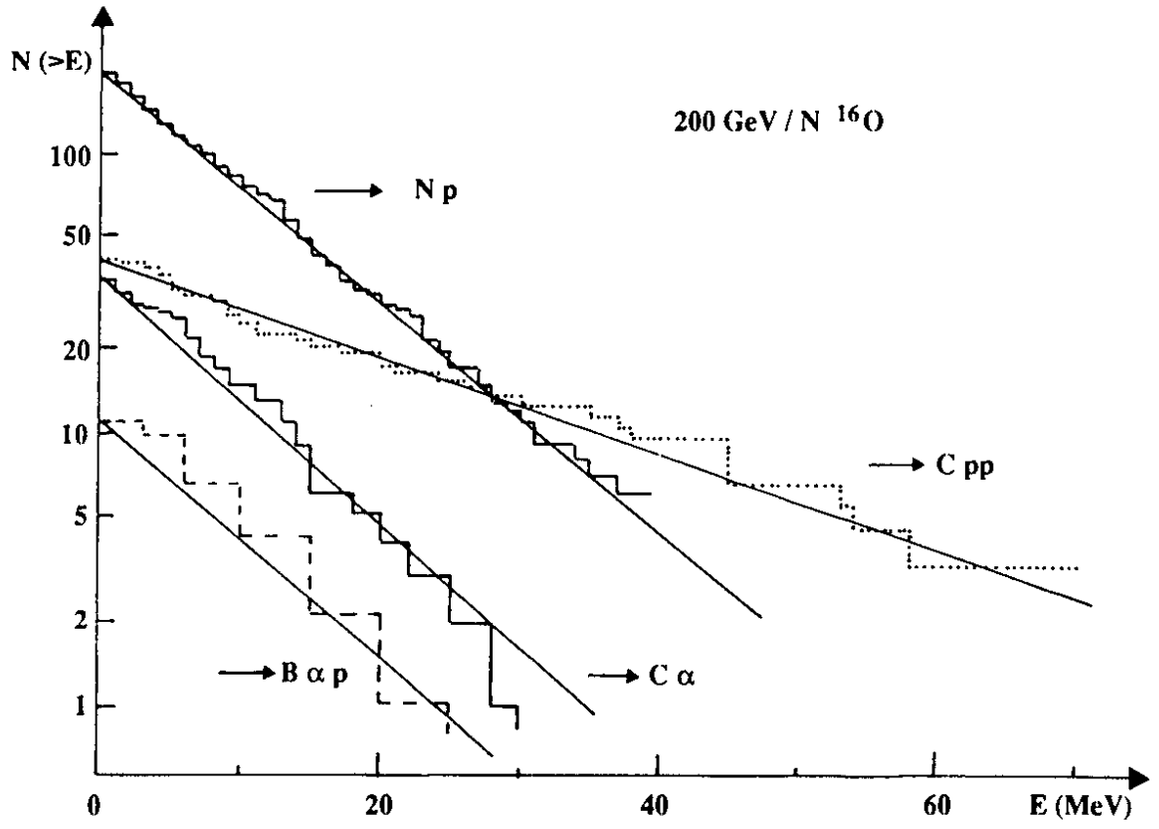
N (>E)
200 GeV / N ^{16}O
100
50
20
10
5
2
1
N p
C pp
B α p
C α
0
20
40
60
E (MeV)

Fig. 15

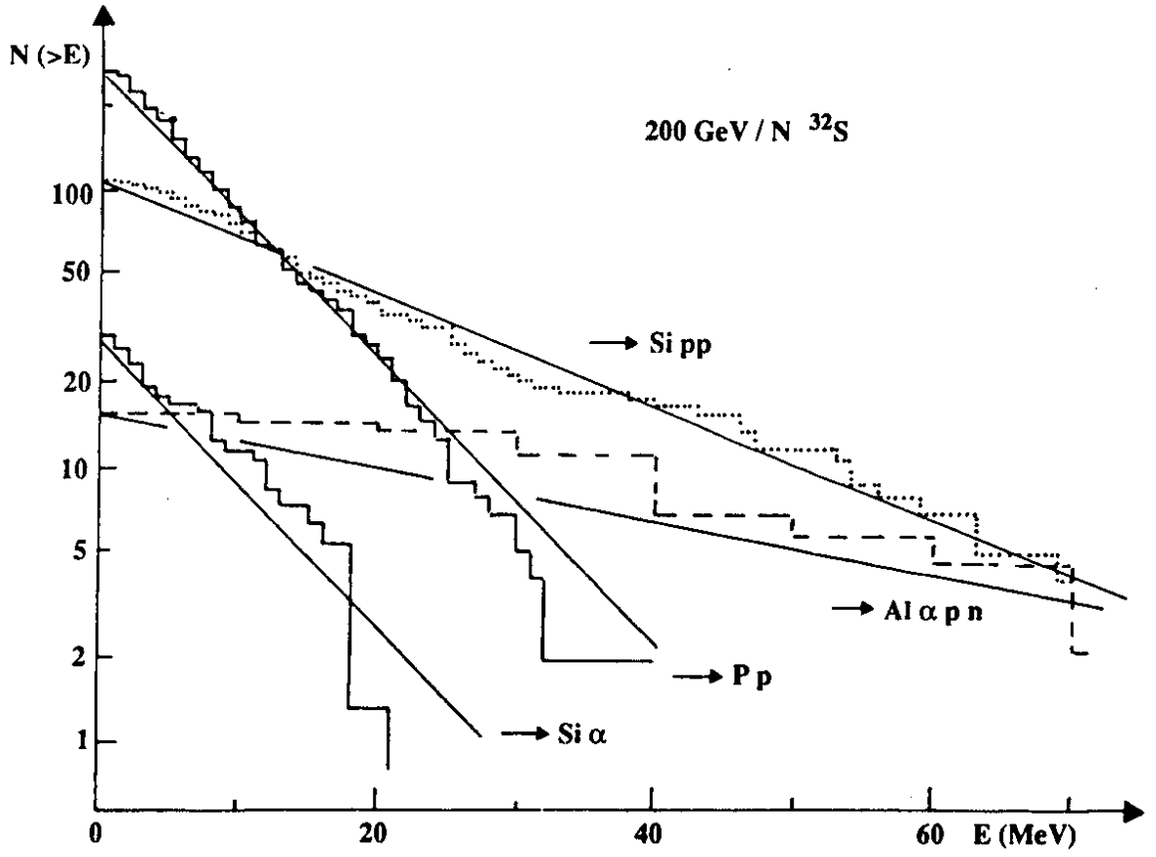
N (>E)
200 GeV / N ^{32}S
100
50
20
10
5
2
1
Si pp
Al α p n
P p
Si α
0
20
40
60
E (MeV)

Fig. 16

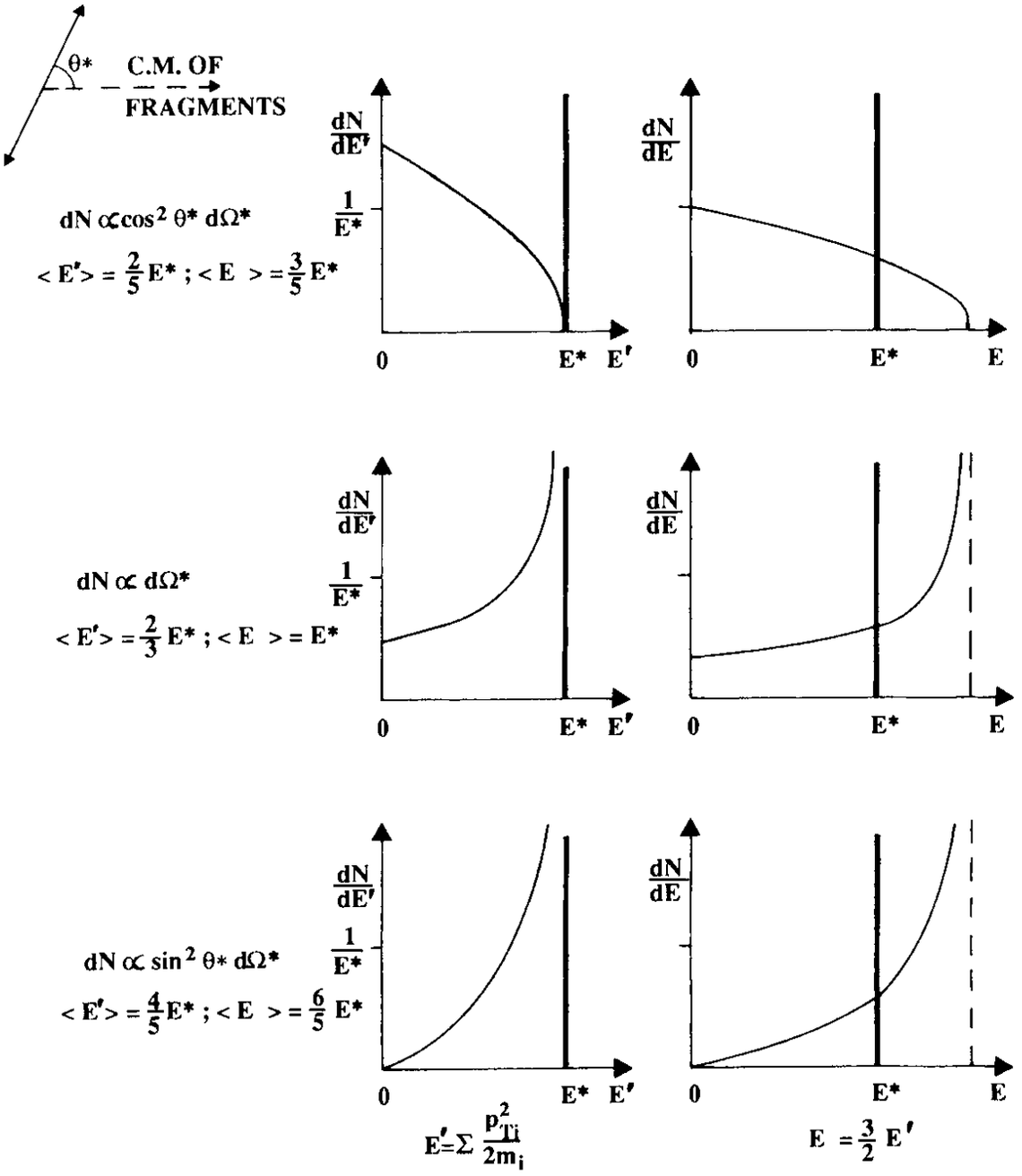
θ*
C.M. OF FRAGMENTS
dN ∝ cos² θ* dΩ*
< E' > = 2/5 E* ; < E > = 3/5 E*
dN/dE'
1/E*
0
E*
E'
dN/dE
E
dN ∝ dΩ*
< E' > = 2/3 E* ; < E > = E*
dN ∝ sin² θ* dΩ*
< E' > = 4/5 E* ; < E > = 6/5 E*
E' = Σ p²Ti / 2mi
E = 3/2 E'

Fig. 17

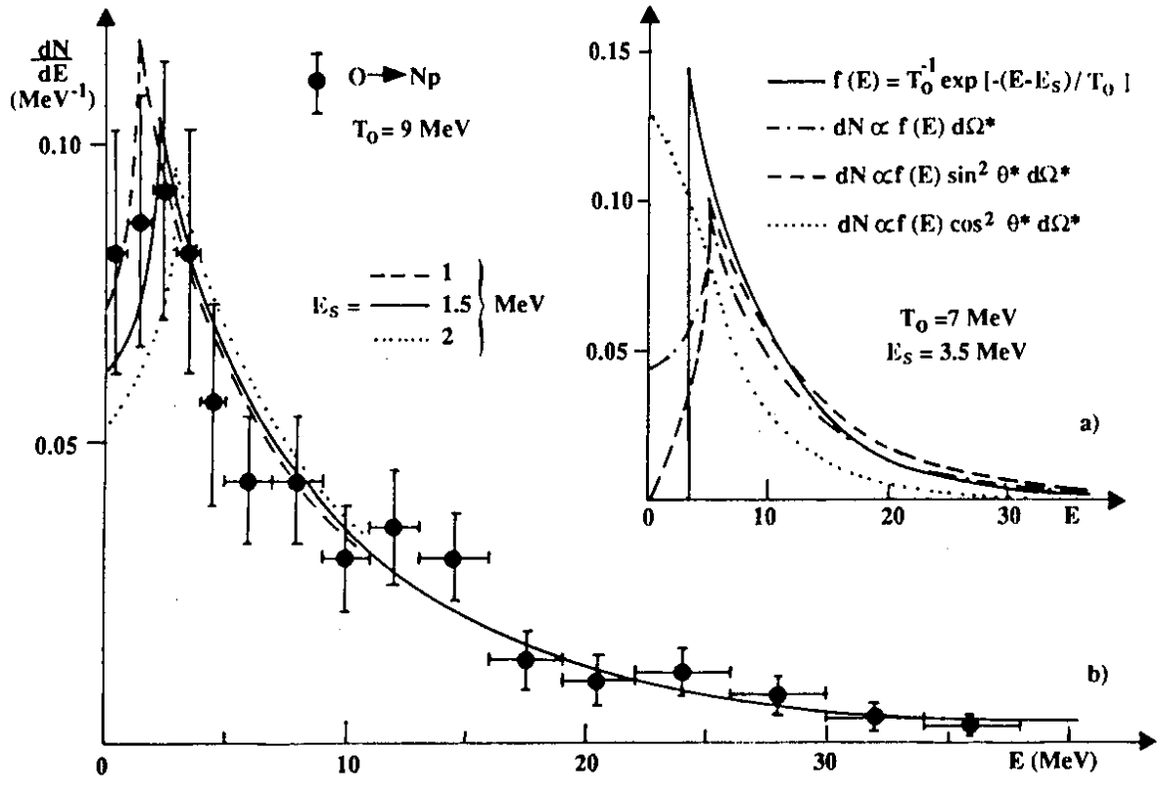
dN/dE (MeV⁻¹)
0.10
0.05
O→Np
T₀ = 9 MeV
E_S = 1
1.5
2
MeV
0
10
20
30
E (MeV)
b)
0.15
0.10
0.05
f (E) = T₀⁻¹ exp [-(E-E_S)/ T₀]
dN ∝ f (E) dΩ*
dN ∝f (E) sin² θ* dΩ*
dN ∝f (E) cos² θ* dΩ*
T₀ =7 MeV
E_S = 3.5 MeV
a)
0
10
20
30
E

Fig. 18

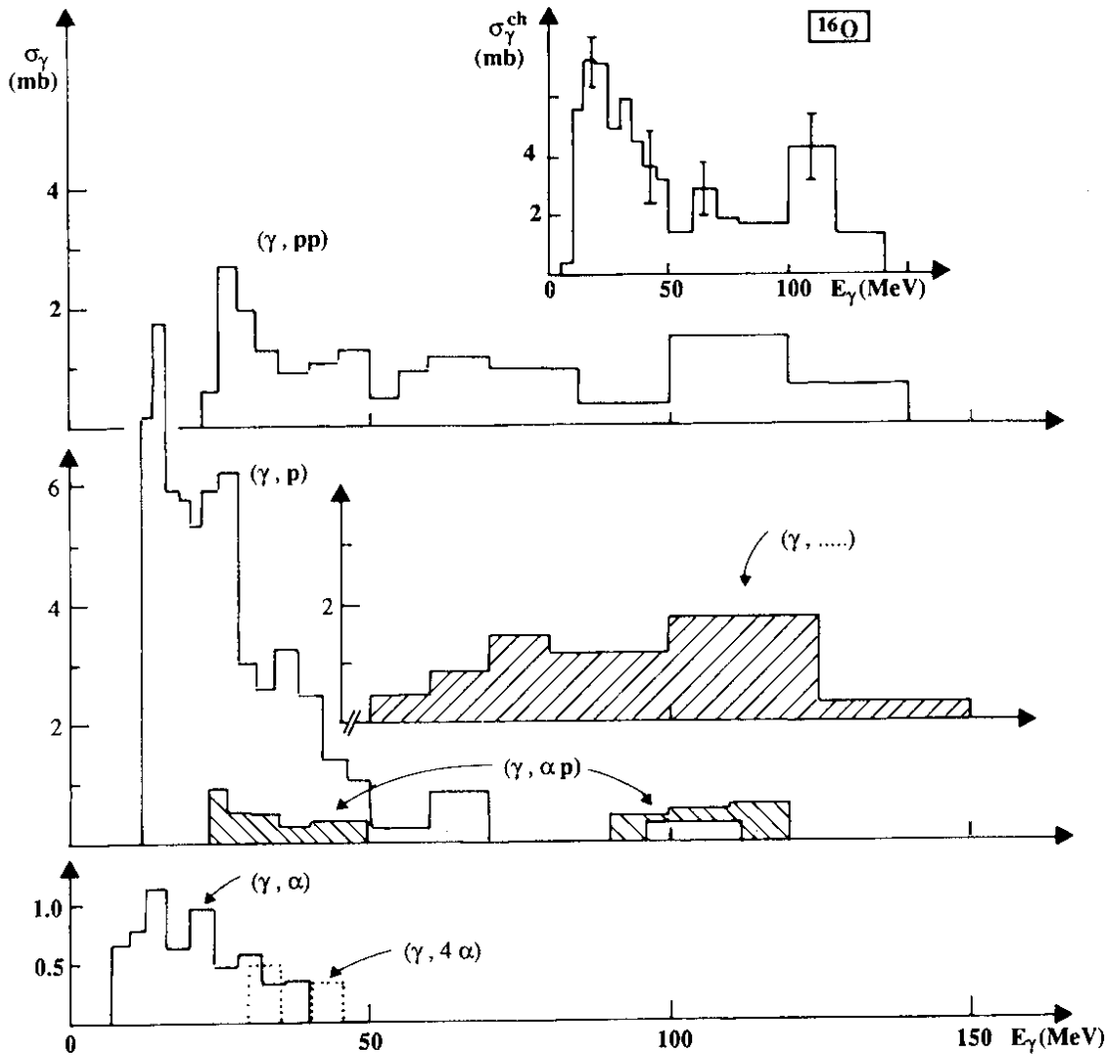
σ_γ (mb)
σ_γ^{ch} (mb)
^{16}O
(γ , pp)
(γ , p)
(γ , ...)
(γ , α p)
(γ , α)
(γ , 4 α)
E_γ(MeV)

Fig. 19

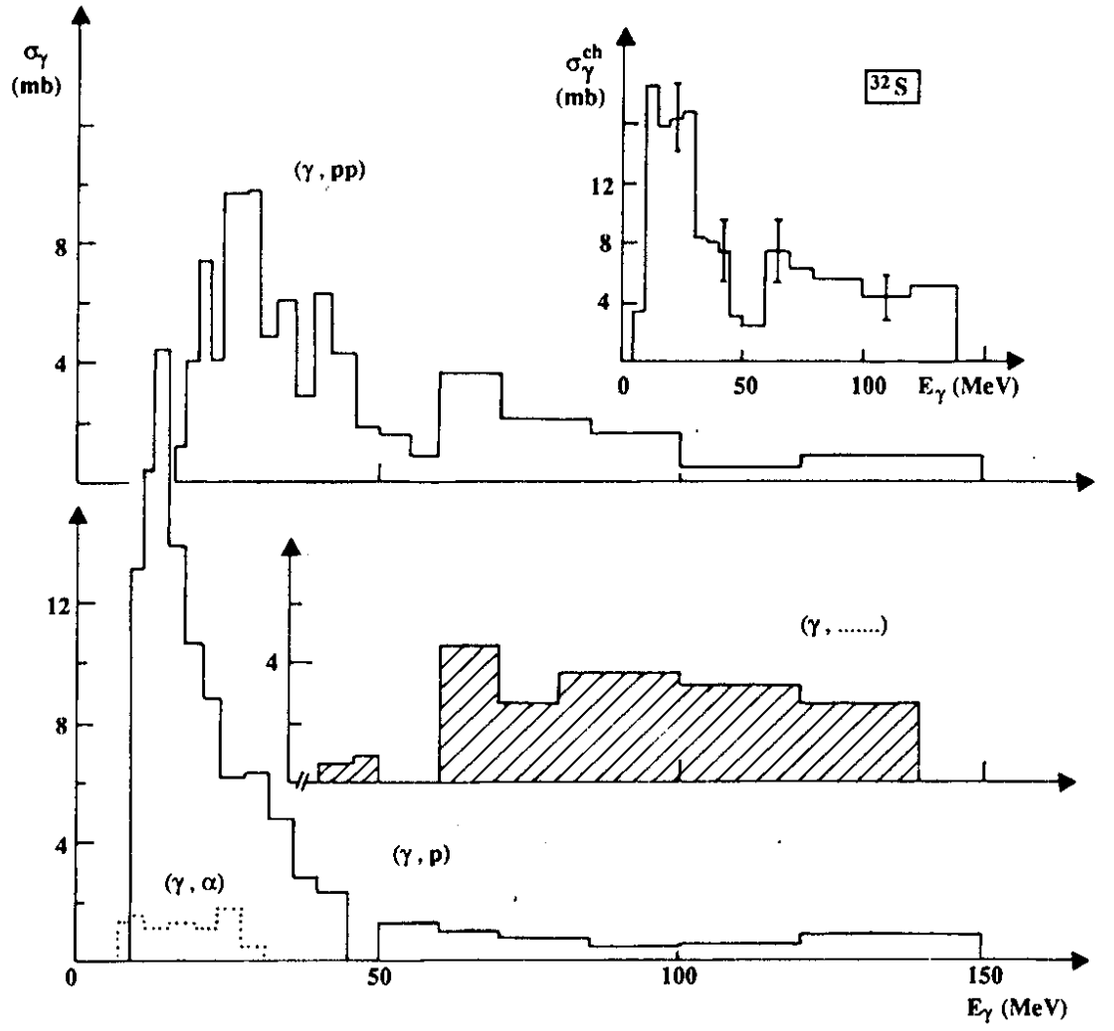

Fig. 20